Quantifying and Understanding Forced Changes to Unforced Modes of Atmospheric Circulation Variability over the North Pacific in a Coupled Model Large Ensemble

JOHN P. O'BRIEN[a,b] AND CLARA DESER[a]

[a] Climate and Global Dynamics Division, National Center for Atmospheric Research, Boulder, Colorado
[b] Climate and Ecosystem Sciences Division, Lawrence Berkeley National Laboratory, Berkeley, California

(Manuscript received 11 February 2022, in final form 29 July 2022)

ABSTRACT: While much attention has been given to understanding how anthropogenic radiative forcing influences the mean state of the climate system, far less scrutiny has been paid to how it may modulate naturally occurring modes of variability. This study investigates forced changes to unforced modes of wintertime atmospheric circulation variability and associated impacts on precipitation over the North Pacific and adjacent regions based on the 40-member Community Earth System Model version 1 Large Ensemble across the 1920–2100 period. Each simulation is subject to the same radiative forcing protocol but starts from a slightly different initial condition, leading to different sequences of internal variability. Evolving forced changes in the amplitude and spatial character of the leading internal modes of 500-hPa geopotential height variability are determined by applying empirical orthogonal function analysis across the ensemble dimension at each time step. The results show that the leading modes of internal variability intensify and expand their region of influence in response to anthropogenic forcing, with concomitant impacts on precipitation. Linkages between the Pacific and Atlantic sectors, and between the tropics and extratropics, are also enhanced in the future. These projected changes are driven partly by teleconnections from amplified ENSO activity and partly by dynamical processes intrinsic to the extratropical atmosphere. The marked influence of anthropogenic forcing on the characteristics of internal extratropical atmospheric circulation variability presents fundamental societal challenges to future water resource planning, flood control, and drought mitigation.

KEYWORDS: El Nino; ENSO; Pacific-North American pattern/oscillation; Teleconnections; Climate variability; Internal variability

1. Introduction

Anthropogenic emissions of well-mixed greenhouse gases, aerosols and other radiatively active constituents are causing rapid and measurable changes to the mean state of the global climate system despite uncertainty arising from complex physical processes (IPCC 2007, 2013, 2021). While much attention has been given to understanding these mean-state changes, far less scrutiny has been paid to how such emissions modulate the character of internally generated climate variability. Fundamentally, the coupled ocean–atmosphere–land system is governed by nonlinear dynamics, which gives rise to chaotic behavior that defines a distribution of possible outcomes about its mean state (Lorenz 1963). Such internally generated variability is an inherent feature of the climate system and places practical limits on predictability across a range of space and time scales (Branstator and Teng 2010; Deser et al. 2012a; DelSole and Tippett 2018).

An important source of internally generated climate variability derives from fluctuations in recurrent large-scale patterns of atmospheric circulation known as teleconnections (Wallace and Gutzler 1981; Barnston and Livezey 1987; Feldstein 2000; Feldstein and Franzke 2017). These atmospheric modes of variability arise from internal atmospheric dynamics (e.g., Branstator and Teng 2017) as well as coupled ocean–atmosphere (DeWeaver and Nigam 2004; Stan et al. 2017; Dong et al. 2018; Thomson and Vallis 2018) and land–atmosphere (Teng et al. 2019) interactions, and are important modulators of regional weather and climate on subseasonal to decadal time scales (Ropelewski and Halpert 1987; Leathers et al. 1991; Hurrell 1995; Diaz et al. 2001; Fasullo et al. 2020). Well-studied examples include the Pacific–North American (PNA; Wallace and Gutzler 1981) pattern, North Atlantic Oscillation (NAO; Hurrell et al. 2003), and teleconnections arising from El Niño–Southern Oscillation (ENSO; Bjerknes 1969).

It is likely that these intrinsic structures of variability will undergo changes in amplitude, spatial pattern and temporal behavior as a result of anthropogenic forcing (e.g., Branstator and Selten 2009; Shepherd 2014; Deser et al. 2018), and their remote linkages and climate impacts may change as well. For example, recent studies indicate that the PNA pattern may amplify (Chen et al. 2018) and its center-of-action may shift northeastward (Michel et al. 2020) in response to anthropogenic climate change. NAO variability is also expected to increase in a warming climate; however, model dependence and multidecadal sampling fluctuations impart considerable

Denotes content that is immediately available upon publication as open access.

Supplemental information related to this paper is available at the Journals Online website: https://doi.org/10.1175/JCLI-D-22-0101.s1.

Corresponding author: John P. O'Brien, jpobrien@ucar.edu

DOI: 10.1175/JCLI-D-22-0101.1

uncertainty and may obscure such forced changes (Visbeck et al. 2001; Gillett et al. 2003; Deser et al. 2017a; Huang et al. 2018; McKenna and Maycock 2021). The interaction of teleconnection patterns with mean-state changes in background flow and stationary and nonstationary wave characteristics [e.g., the Madden–Julian oscillation (MJO)] further complicates their response to anthropogenic forcing (Brandefelt and Körnich 2008; Simpson et al. 2014; Mann et al. 2017; Wills et al. 2019; Zhou et al. 2020).

Despite intense investigation, future changes to the characteristics of internally generated ENSO variability remain uncertain (e.g., Collins et al. 2010; Kohyama et al. 2018; Bellenger et al. 2014; Cai et al. 2020; Wengel et al. 2021), although there is a growing consensus that ENSO-related tropical precipitation variability will increase in a warmer climate (Power et al. 2013; Cai et al. 2014; Huang and Xie 2015; Cai et al. 2020; Yun et al. 2021), impacting ENSO-induced teleconnections (Zhou et al. 2014; Drouard and Cassou 2019; Beverley et al. 2021). A recent study by Cai et al. (2021) shows that there is high intermodel agreement that ENSO sea surface temperature (SST) variability will increase in the twenty-first century compared to the twentieth century, but only when sampling fluctuations due to limited record length are adequately considered. However, model resolution and mean-state biases may affect this conclusion (e.g., Kohyama et al. 2018; Stevenson et al. 2021; Wengel et al. 2021), underscoring the need for improved process-level understanding.

In addition to the myriad physical processes that can complicate a robust quantification of simulated teleconnection patterns and their response to climate change, there are also nonphysical constraints such as model parameterizations and finite computational resources. Moreover, the relatively short observational record hinders a robust statistical assessment of teleconnection properties and possible forced changes thereof, constraining model evaluation efforts (Hawkins and Sutton 2009; Deser et al. 2017a,b; Maher et al. 2018; Deser et al. 2020; Fasullo et al. 2020). The historical climate record is special in that it is the only one we have, or ever will experience; however, it also represents just one realization of an infinite number of ways our climate history could have unfolded (Deser 2020; Mankin et al. 2020). Coupled climate modeling can overcome this limitation through the generation of multiple realizations under identical forcing scenarios with infinitesimal perturbations to the initial conditions. Due to the governing chaotic dynamics, these realizations diverge and their extratropical atmospheric circulation states become largely uncorrelated after a few weeks (Lorenz 1963; Deser et al. 2012b). Such "initial condition" large ensembles (LEs) are intended to span the range of simulated internal variability and allow us to probe alternate realities in which our climate history could have unfolded differently than it has (Tebaldi and Knutti 2007; Deser et al. 2012b). As such, LEs provide an ideal test bed for assessing changes in internal climate variability resulting from external forcing and are being used accordingly (Deser et al. 2020).

A benefit of LEs is the large number of samples of (simulated) internal variability at any given instant in time. This unique attribute of model LEs can be exploited with suitable analysis techniques. For example, teleconnection patterns are often determined through the lens of empirical orthogonal function (EOF) analysis, a statistical technique designed to capture spatially coherent patterns that explain the greatest proportion of temporal variability across the domain of interest (Wallace and Gutzler 1981). However, with an LE, provided there are enough realizations, the EOF approach may be applied over the ensemble dimension rather than the time dimension, allowing a direct assessment of the evolving impact of external forcing on modes of internal variability. This novel technique, known as ensemble-EOFs (Maher et al. 2018) or snapshot-EOFs (SEOFs; Haszpra et al. 2020a), has only recently been introduced to climate science and is particularly well suited to the analysis of LEs. Since the mean across the ensemble (i.e., the forced response) is removed prior to calculating the SEOFs, only the internal component of variability in each ensemble member at each time step is retained in the analysis. While the forced response to the mean state is removed at each time step, externally forced changes to internal variability are retained. Applications of SEOF analysis to date include the study of forced changes in ENSO and related teleconnection patterns (Maher et al. 2018; Bódai et al. 2020; Haszpra et al. 2020a), the NAO (Herein et al. 2016, 2017), and the Arctic Oscillation (AO; Haszpra et al. 2020b).

In this study, we apply the SEOF methodology to quantify and understand evolving forced changes in intrinsic patterns of wintertime atmospheric circulation variability over the North Pacific and concomitant changes in precipitation, including those over North America, during the period 1920–2100 as simulated by the 40-member LE conducted with the fully coupled Community Earth System Model version 1 (CESM1; hereafter CESM1-LE; Kay et al. 2015). We further decompose these forced changes into their tropical and extratropical origins via ensemble linear correlations with the leading SEOF modes of internal tropical Pacific SST variability. We also assess the influence of anthropogenic forcing on linkages between internal circulation variability over the North Pacific and North Atlantic, and the role of the tropics in mediating such connections. Finally, we quantify the relative magnitudes of forced changes in modes of internal variability versus forced changes in the mean state. We also discuss the extent to which these modes of variability are symmetric with respect to polarity.

The remainder of the paper is organized as follows. In section 2, we describe the data and analysis methods. In section 3, we present our results, including a validation of our approach to isolating tropical versus extratropical sources of forced changes in internal variability. In section 4, we synthesize and discuss our findings, including implications for future environmental change and human systems.

2. Data and methods

a. Data

This study employs the 40-member CESM1-LE conducted at a spatial resolution of 1° in both latitude and longitude (Kay et al. 2015). The historical portion of these simulations (1920–2006) is subject to observed natural and anthropogenic radiative forcings, while the future period (2007–2100) uses the RCP8.5 emissions scenario, which is characterized by high rates of fossil fuel consumption with no climate mitigations (Riahi et al. 2011; van Vuuren et al. 2011). Each ensemble member is given a random perturbation to the initial atmospheric temperature field (order of 10^{-14} K), which serves to create ensemble spread due to the internal chaotic dynamics of the coupled system (Lorenz 1963; Deser et al. 2012a). Once the memory of the initial conditions is lost, the individual members follow independent sequences of internal variability superimposed upon a common forced response. With a sufficient number of ensemble members, the ensemble-mean represents the externally forced response at any given time (Milinski et al. 2020).

We analyze the following monthly output fields from the CESM1-LE: 500-hPa geopotential height (Z500), total precipitation (large-scale plus convective; PRECT), and surface temperature (TS); the latter is equivalent to SST at oceanic grid boxes. All quantities are seasonally averaged over boreal winter December–February (DJF). We also employ a 2600-yr atmosphere-only control simulation conducted as part of the CESM1-LE Project. This simulation uses preindustrial (1850) radiative forcing conditions and monthly varying SST and sea ice concentration (SIC) climatologies taken from the 1800-yr fully coupled preindustrial control simulation (see Kay et al. 2015 for further information).

b. *Modes of variability*

We apply SEOF analysis to DJF Z500 anomalies over the extratropical (20°–90°N) North Pacific (NPac: 110°–260°E) and North Atlantic (NAtl: 80°W–10°E) domains, and to DJF SST anomalies over the tropical Pacific (TPac: 35°S–35°N, 140°–295°E). These domains are outlined in Figs. S1 and S2 in the online supplemental material. We consider the three leading Z500 SEOFs over the NPac region, which we shall refer to as NPac_Z500_SEOF1, NPac_Z500_SEOF2, and NPac_Z500_SEOF3. As will become apparent, the first mode is equivalent to the Pacific–North American pattern (PNA; Barnston and Livezey 1987), the second mode to the North Pacific Oscillation (NPO; Linkin and Nigam 2008), and the third mode to the east Pacific pattern (EPP; Barnston and Livezey 1987; Yuan et al. 2015). We also consider the leading Z500 SEOF over the NAtl region (NAtl_Z500_SEOF1), which represents the NAO (Hurrell et al. 2003), and the two leading SST SEOFs over the TPac region. TPac_TS_SEOF1 represents the canonical ENSO pattern, whose positive phase is closely associated with eastern Pacific El Niño events (Kao and Yu 2009), and TPac_TS_SEOF2, in its positive phase, is synonymous with central Pacific El Niño (aka Modoki) events (Capotondi et al. 2015). Note that while we refer to TPac_TS_SEOF1/2 as east Pacific/central Pacific (Modoki) ENSO, respectively, it should be recognized that these are only naming conventions useful for referring to specific parts of the nonlinear continuum that is ENSO (Takahashi et al. 2011; Dommenget et al. 2013; Williams and Patricola 2018; also see row 1 of Fig. S3). All four modes of Z500 variability considered in this study, and their associated impacts on precipitation, are realistically simulated in the CESM1-LE, as shown in Figs. S6 and S7 of Guo et al. (2019) and Fig. 3 of Deser et al. (2017b) based on traditional space–time EOF analysis over the historical period (see also Fasullo et al. 2020). The ENSO modes are also generally well represented in terms of amplitude and spectral characteristics, with a slight westward extension of their equatorial Pacific SST anomalies due to the well-known mean state bias of the cold tongue (see Capotondi et al. 2020; Fasullo et al. 2020; Wu et al. 2022).

c. *Snapshot-EOF analysis*

An ever-increasing concern with applying conventional EOF analysis to climate data in the time domain is the issue of non-stationarity resulting from anthropogenically forced climate change (Milly et al. 2008; AghaKouchak et al. 2013; Sarhadi et al. 2018). Non-stationarity occurs in the presence of aperiodic or time-dependent climate forcings, which results in time-dependent statistics. Thus, in the case of traditional EOF analysis, one must always subjectively choose the time window over which to calculate the EOF, which in the presence of nonstationary data can result in time-dependent representations of the phenomenon in question.

Here, we compute the leading modes of variability discussed in section 2b using the SEOF approach. We calculate the SEOFs across the ensemble dimension of a four-dimensional data object consisting of ensemble, time, latitude, and longitude dimensions. By definition, EOF analysis operates on data from which the mean has been removed; in the case of SEOF analysis, the ensemble-mean (i.e., the forced response) is removed from the data at each time step, leaving only the internal component for analysis. In addition, as is standard with EOF analysis, the data are weighted by the square root of the cosine of the latitude to account for converging longitudes and decreasing grid areas approaching the poles. The resulting SEOFs, computed independently for each time step across the 40 realizations of the CESM1-LE, describe the leading modes of unforced variability at a given instant in time (Drótos et al. 2015; Herein et al. 2017). We verify that no mode-mixing occurs among the SEOFs and that higher-order modes are well separated according to the North test (Fig. S4; North et al. 1982).

For added robustness, we increase the number of samples used in each SEOF calculation from 40 to 200 by including all winters within a 5-yr running time window (note that we do not apply a running mean to the data; rather, we pool the 5 discrete winters within the 5-yr time window). This approach assumes the climate is roughly stationary with respect to external forcings across the windowed period, which is a reasonable assumption in this application. We then assign the resulting SEOFs to the year on which the window is centered. For example, the first SEOF calculation includes the years 1921–25 and is assigned to the year 1923. Therefore, for the full 1921–2100 time period, we calculate 5-yr windowed SEOFs whose central years span from 1923 to 2098 (176 central dates in total).

Like traditional space–time EOF analysis, which results in mutually orthogonal components in both space (the EOFs) and time [the principal components (PCs)], the equivalent

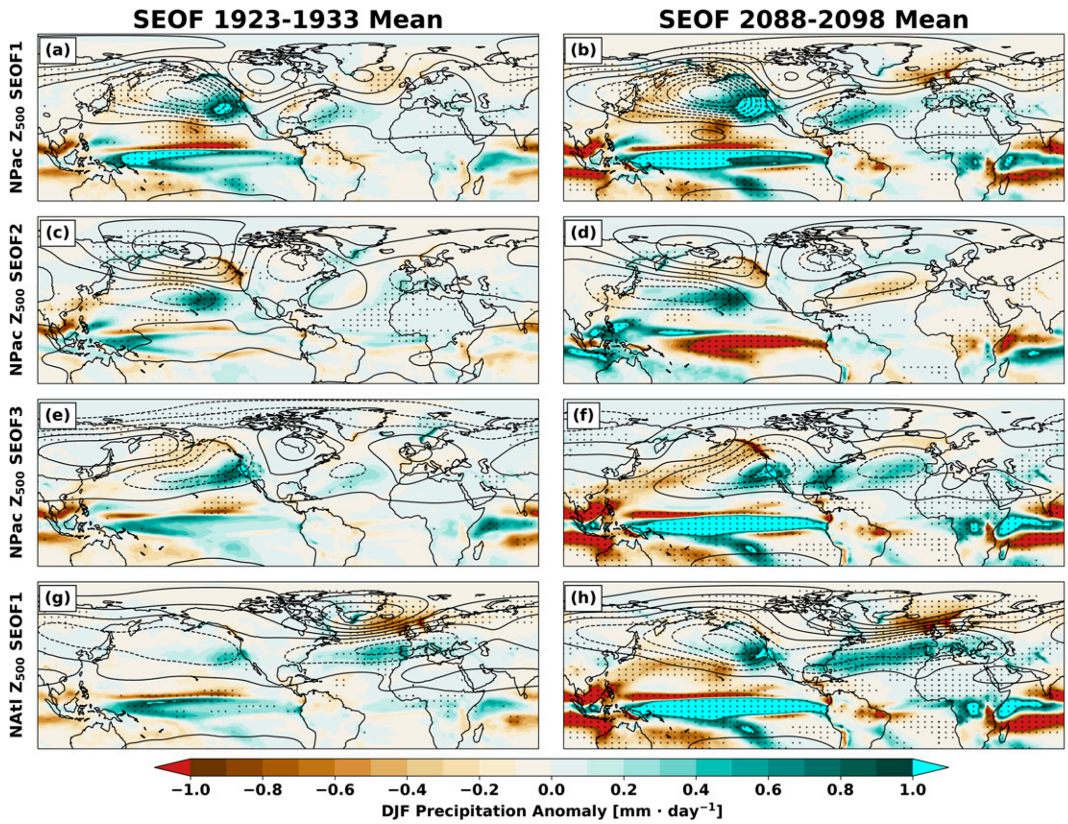

FIG. 1. DJF regression maps of precipitation (mm day^{-1}; color shading) and Z500 (contour interval = 10 m; negative values shown as dashed contours) during (left) 1923–33 and (right) 2088–98 for (a)–(f) the three leading SEOFs of North Pacific Z500 variability and (g),(h) the leading SEOF of North Atlantic Z500 variability. Stippling indicates statistically significant values (0.01 significance level) in at least 7 of 10 years. See text for details of the SEOF methodology and Fig. S1 for the SEOF domains.

space-ensemble SEOF components are likewise mutually orthogonal in both the space and ensemble dimensions. Each snapshot principal component (SPC) describes the amplitude and sign of the corresponding SEOF in each ensemble member. We create global regression maps for each standardized SPC by linearly regressing anomalies (departures from the ensemble mean) of a particular field (Z500, PRECT, or TS) in each ensemble member onto the SPC, and repeat this procedure for each windowed time step. Statistical significance for each SEOF (unless otherwise noted) is indicated by stippling where the p value on the SPC ensemble regression is less than or equal to the 0.01 significance level. In addition, we also employ a procedure for multiple hypothesis testing to control for false positive discoveries ($q^* = 0.01$) to ensure the robustness of statistically significant patterns (Benjamini and Hochberg 1995). For all map-view figures, statistical significance stippling always corresponds to the color-filled field.

3. Results

a. Forced changes in variability

Figure 1 displays regression maps of Z500 (contours) superimposed upon precipitation (color shading) for each of the four extratropical Z500 SEOFs defined in section 2. The left column shows results averaged over the first 10 years of the analysis period (1923–33) and the right column shows results averaged over the last 10 years (2088–98). While the phase of each mode is arbitrary, we have chosen to display them such that the associated precipitation anomalies over the equatorial Pacific are positive, with the exception of NPac_Z500_SEOF2, which is defined to be consistent with its correlation to central Pacific Modoki as discussed in greater detail below. In the early period (left column), NPac_Z500_SEOF1 (PNA; Fig. 1a) shows a wave-like circulation structure with a prominent trough centered over the North Pacific just south of the Aleutian peninsula. NPac_Z500_SEOF2 (NPO; Fig. 1c) is characterized by a meridionally oriented dipole structure featuring a zonally elongated trough centered over the subtropical Pacific with an associated ridge centered over the Bering Strait region. NPac_Z500_SEOF3 (EPP; Fig. 1e) displays a well-developed trough over the eastern North Pacific oriented such that it represents a pathway for subtropical moisture transport to the western United States, with an associated ridge centered over the Hudson Bay region. Finally, NAtl_Z500_SEOF1 (NAO; Fig. 1g) most prominently depicts a meridionally oriented dipole structure centered over the North Atlantic.

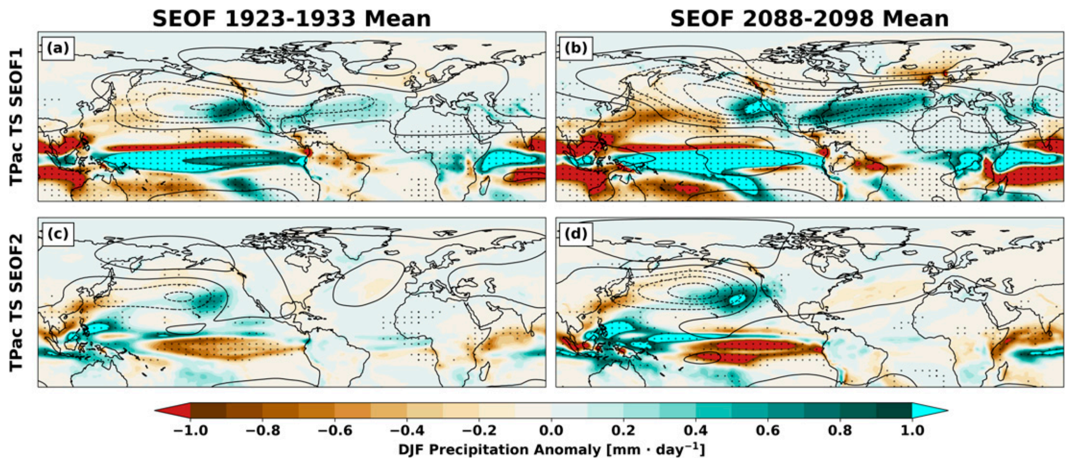

FIG. 2. As in Fig. 1, but for the first two SEOFs of tropical Pacific SST variability (see Fig. S2 for the SEOF domains).

The right column of Fig. 1 displays the transformation each mode undergoes by the end of the twenty-first century. Of the three NPac modes, NPac_Z500_SEOFs 1 and 3 both show a pronounced amplification/deepening of their respective circulation features as well as an enhancement of their associated precipitation anomalies over the North Pacific and along the U.S. West Coast. NPac_Z500_SEOF3 is a mode that has received less attention; however, we find that it plays an increasingly important role in a future warmer climate. NPac_Z500_SEOF3 is most prominently associated with subtropical moisture transport originating near the Hawaiian Islands (Figs. 1e,f). Moisture laden storms originating in this region are commonly known as atmospheric rivers (ARs), specifically, ARs of the "Pineapple Express" variety (Rutz et al. 2019; O'Brien et al. 2020). Figure 1f indicates that in a future warmer climate, this mode is both amplified and shifted southeastward, suggesting a greater likelihood for future AR activity for the western United States. This is consistent with previous studies that show AR frequency and intensity increase globally with climate warming (Payne et al. 2020), with disproportionate increases in the Pacific basin (O'Brien et al. 2022), and in particular California (Gershunov et al. 2019; Rhoades et al. 2021). NPac_Z500_SEOF2 shows more subdued changes, with modest strengthening of the trough over the central North Pacific and associated precipitation increase. In addition, this mode develops a more prominent semi-hemispherical wave train character spanning from the North Pacific to the North Atlantic arcing over the polar region. NAtl_Z500_SEOF1 amplifies considerably by the end of the twenty-first century, not only over the Atlantic sector but even more conspicuously in its connection to the PNA over the North Pacific, with an associated enhancement of precipitation over the western and southeastern United States. (For a more detailed look at the circulation patterns and their statistical significance, see Fig. S1.)

Common to all the Z500 SEOF modes is the striking increase in their associated amplitudes of tropical Indo-Pacific precipitation variability from the early twentieth century to the late twenty-first century (cf. left and right columns of Fig. 1). This suggests that enhanced tropical precipitation variability indicative of stronger ENSO activity in the future may be playing a role in driving the changes seen in the extratropical circulation and hydroclimate patterns. To evaluate this supposition, we calculate the SEOFs corresponding to the first two leading modes of tropical Pacific (TPac) SST variability, which together explain approximately 70% of the interannual SST variability at each time step (note, that like SEOFs themselves, the variance they explain is also an implicit function of time: see Fig. 3). Figure 2 displays the precipitation and Z500 regression maps for each TPac SEOF mode in the early (1923–33) and late (2088–98) periods. In its positive phase, TPac_TS_SEOF1 bears resemblance to east Pacific (EP) El Niño and TPac_TS_SEOF2 to central Pacific El Niño (Modoki), as shown in Fig. S2, although there is not a unique one-to-one mapping (see section 4 for additional discussion of the nonlinear interactions between these modes.)

In the early period, TPac_TS_SEOF1 displays a zonally elongated pattern of below normal Z500 heights over the North Pacific extending into the North Atlantic, with opposite-signed anomalies over Canada and the subpolar North Atlantic, while TPac_TS_SEOF2 shows a meridionally oriented dipole structure over the North Pacific resembling the NPO (Figs. 2a,c, respectively); both Z500 patterns are statistically significant (Fig. S5). TPac_TS_SEOF1 is associated with positive precipitation anomalies over the western half of the equatorial Pacific and Indian Oceans typical of the warm phase of ENSO (Fig. 2a), while TPac_TS_SEOF2 is accompanied by weak negative precipitation anomalies over the central equatorial Pacific (Fig. 2c).

The most pronounced end-of-century changes are seen for TPac_TS_SEOF1, which shows enhanced variability in tropical precipitation, a deepened and wider extratropical circulation response that spans nearly the entire Northern Hemisphere, and an amplified extratropical hydroclimate response most apparent over the western and southeastern United States extending out across the North Atlantic and into western Europe (Fig. 2b). End-of-century changes in TPac_TS_SEOF2 include intensified and slightly eastward-shifted tropical Pacific precipitation variability, along with a commensurate amplification and eastward shift of the North Pacific trough and associated precipitation signal off the western United States (Fig. 2d).

These changes indicate that early in the record, the regional western U.S. response to events associated with TPac_TS_SEOF2 is largely insignificant (Fig. 2c), consistent with the findings of previous studies (Ashok et al. 2007; He et al. 2021). However, by the end of the twenty-first century, these events are intensified, leading to a stronger and statistically significant hydroclimate response in the western United States, particularly over California (Fig. 2d). Note that while we focus on describing the changes associated with the positive phase of each mode, the SEOFs presented here are symmetric by construction and therefore describe variability of both polarities. As such the negative phase impacts are also implicit in our descriptions. For example, considering TPac_TS_SEOF1 (EP ENSO), while the positive phase (El Niño) shows increasing precipitation over the central/east Pacific, western and southeastern North America, and western Europe, the negative phase (La Niña) will have equal and opposite impacts. The implicit symmetry in our study is a consequence of the linear regression used in representing the SEOFs and thus does not capture any asymmetries known to exist for ENSO (e.g., Hoerling et al. 1997; Frauen and Dommenget 2010; Takahashi et al. 2011; Dommenget et al. 2013). For an accounting of nonlinear asymmetric impacts associated with ENSO, see Figs. S14–S17 as well as Patricola et al. (2020).

Overall, Fig. 2 indicates that ENSO-related tropical precipitation variability in the CESM1-LE increases substantially in a future warmer climate, along with associated atmospheric teleconnections and hydroclimate impacts across much of the Northern Hemisphere. The similarity between the changes depicted in Figs. 1 and 2 suggest that, ENSO forcing will impart a more pronounced signature on the extratropical circulation modes and exert a greater influence on global weather and climate toward the end of the twenty-first century. This is most prominently seen in NAtl_Z500_SEOF1 (NAO) which displays end-of-century precipitation and atmospheric anomaly patterns that are nearly identical to those associated with TPac_TS_SEOF1 for the same time period (cf. Figs. 1h and 2b). This is a particularly significant change as it suggests that regions like western Europe, which historically have seen minimal impacts from ENSO events, in particular the positive El Niño phase, will increasingly be subject to atmospheric perturbations arising from east Pacific SST variability via a novel transatlantic teleconnection. This future amplified teleconnection from the tropical Pacific to the North Atlantic has been recently documented in CMIP5 models (Müller and Roeckner 2008; Fereday et al. 2020), and may be related to the eastward shift of El Niño events in a warmer climate (Williams and Patricola 2018; Zhang et al. 2019). Together this suggests a greater ENSO–NAO teleconnection in the future with potential El Niño impacts to western Europe that are without historical precedent (see also Drouard and Cassou 2019).

Figure 3 shows the fractions of variance explained as well as the total domain variance (red curve; right vertical axis) by each of the SEOF modes as a function of time. Total domain variance increases substantially in the TPac and NPac domains while only rising modestly in the NAtl domain. The increase in total domain variance is mostly reflected in the fractional variance explained by the leading mode in each domain. That is, it is only the leading mode in each domain that shows an increase in their fractional variance explained, which implies that these modes have and will continue to dominate the contribution to overall atmospheric/oceanic variability in their respective regions of influence. For the lower-order modes fractional variance explained across time remains relatively constant. However, because total variance increases in each domain, each individual mode accounts for more total variance across time. It is interesting to note the apparent leveling off in the total variance in the TPac domain. This could indicate a point of saturation in the region that may be related to an asymmetric background warming which reduces zonal and meridional temperature gradients, which are critical for ENSO-related processes (Lindzen and Nigam 1987; Back and Bretherton 2009). As a companion to Fig. 3, Fig. S4 shows the associated North Test errors (North et al. 1982) for each of the individual SEOF modes to establish their separability across time.

To explicitly evaluate the time-varying changes in tropical–extratropical teleconnections, we calculate the ensemble correlations of the extratropical SPCs against the two tropical SPCs. Figure 4a shows the ensemble correlations of the extratropical Z500 modes with TPac_TS_SEOF1 (EP El Niño), while Fig. 4b shows those with TPac_TS_SEOF2 (El Niño Modoki). Reflecting what can be visually inferred from Figs. 1 and 2, tropical–extratropical correlations between ENSO and the extratropical Z500 modes increase in a future warmer climate (Fig. 4). In the 1920s, TPac_TS_SEOF1 is most highly correlated with NPac_Z500_SEOF1 (PNA) (r values ~ 0.47 on average) which implies TPac_TS_SEOF1 explains approximately 25% of the variability in NPac_Z500_SEOF1; correlations between TPac_TS_SEOF1 and the other Z500 modes are much smaller ($r < 0.3$). By the end of the twenty-first century, TPac_TS_SEOF1 correlations with NPac_Z500_SEOF1 are modestly higher ($r \sim 0.57$), but those with the other Z500 modes change more substantially. For example, Fig. 4a indicates that by the end of the twenty-first century, NPac_Z500_SEOF3 will become just as important (if not more so) to the North Pacific El Niño teleconnection as the PNA. What this suggests is that future strong El Niño events will preferentially excite not only the PNA mode, which is associated with enhanced extratropical cyclone activity (Hoerling and Ting 1994), but also NPac_Z500_SEOF3 (EPP), increasing the probability for enhanced subtropical moisture transport and AR activity.

It is interesting to note that the correlations between TPac_TS_SEOF1 and NPac_Z500_SEOF3 are highly variable during the twentieth century, ranging from <0 to about 0.5 depending on the year, unlike those with NPac_Z500_SEOF1, which remain consistently strong throughout ($r \sim 0.5$; Fig. 4a). This indicates that over the historical period, there is substantial uncertainty as to whether tropical forcing excites both the PNA and EPP teleconnections, or only the PNA. Interestingly, the large variability in the model's historical ENSO–EPP connection mostly disappears by 2050/60, after which NPac_Z500_SEOF3 becomes a quasi-permanent feature of the model's ENSO teleconnection and is excited with equal probability

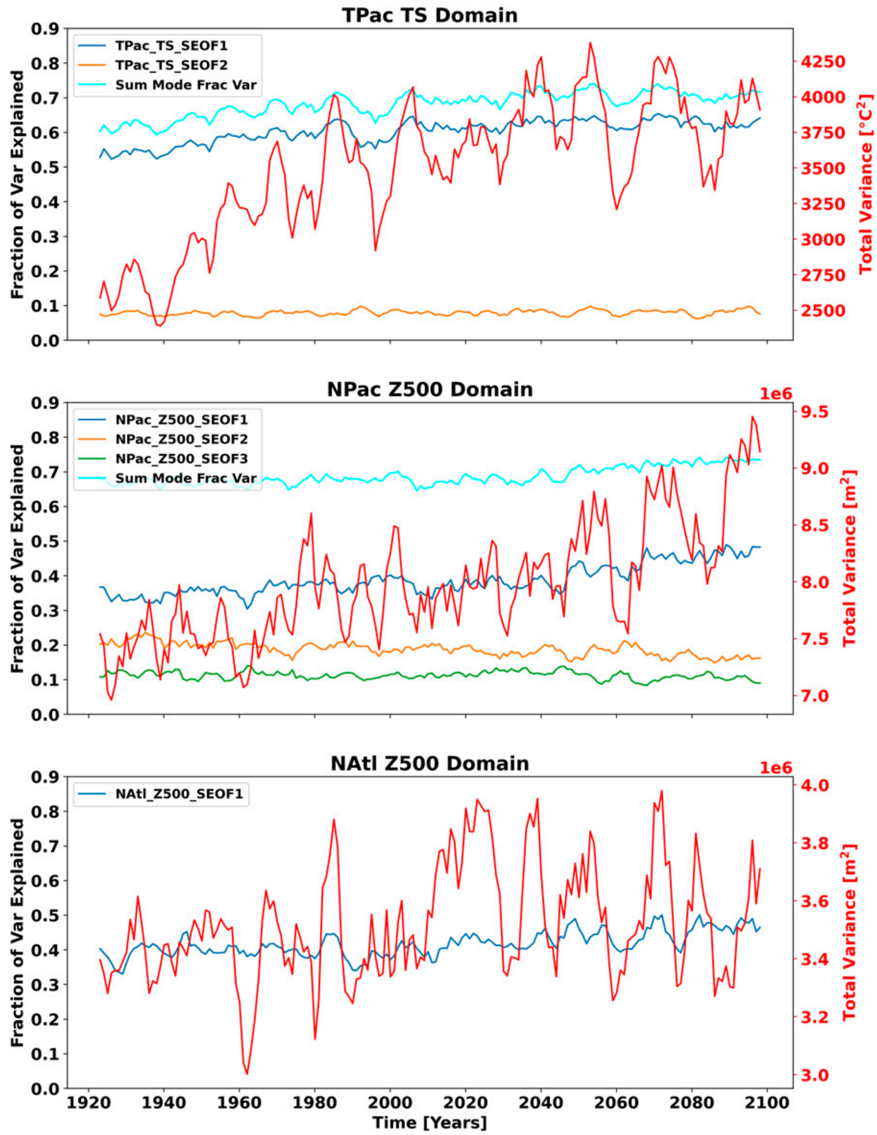

FIG. 3. Total, fractional, and cumulative field variance for the SEOFs over their respective domains. (top) TPac_TS: total variance (red), fractional variance for SEOF1 (blue) and SEOF2 (orange), and their sum (cyan). (middle) NPac_Z500: total variance (red), fractional variance for SEOF1 (blue), SEOF2 (orange), and SEOF3 (green), and their sum (cyan). (bottom) NAtl_Z500: total variance (red) and fractional variance for SEOF1 (blue).

as NPac_Z500_SEOF1. This behavior suggests that the excitation of both the PNA and EPP by strong east Pacific El Niño events may become a regular occurrence toward the end of the twenty-first century. Similarly, the TPac_TS_SEOF1 correlations with NAtl_Z500_SEOF1 become as strong as those with the PNA and the EPP by the middle of the twenty-first century, suggesting the potential for damaging El Niño related flooding in western Europe, similar to that which has occurred in the western United States (Corringham and Cayan 2019).

Figure 4b shows the correlations between the extratropical Z500 modes and TPac_TS_SEOF2 (El Niño Modoki). As was previously noted, there is a strong and robust relationship between TPac_TS_SEOF2 and NPac_Z500_SEOF2 (NPO) that remains effectively unchanged in a future warmed climate. The other extratropical modes show little, if any, correlation with TPac_TS_SEOF2. In addition, only two of the modes, NPac_Z500_SEOF1 (PNA) and NPac_Z500_SEOF3 (EPP), show a statistically significant change in correlation across the simulation period. The relationship with NPac_Z500_SEOF1 becomes slightly more positive, increasing from $r \sim 0.12$ to 0.25. Given that the relationship with NPac_Z500_SEOF1 and western U.S. hydroclimate is to increase precipitation, the increasing positive correlation with TPac_TS_SEOF2 would act to enhance precipitation over the region

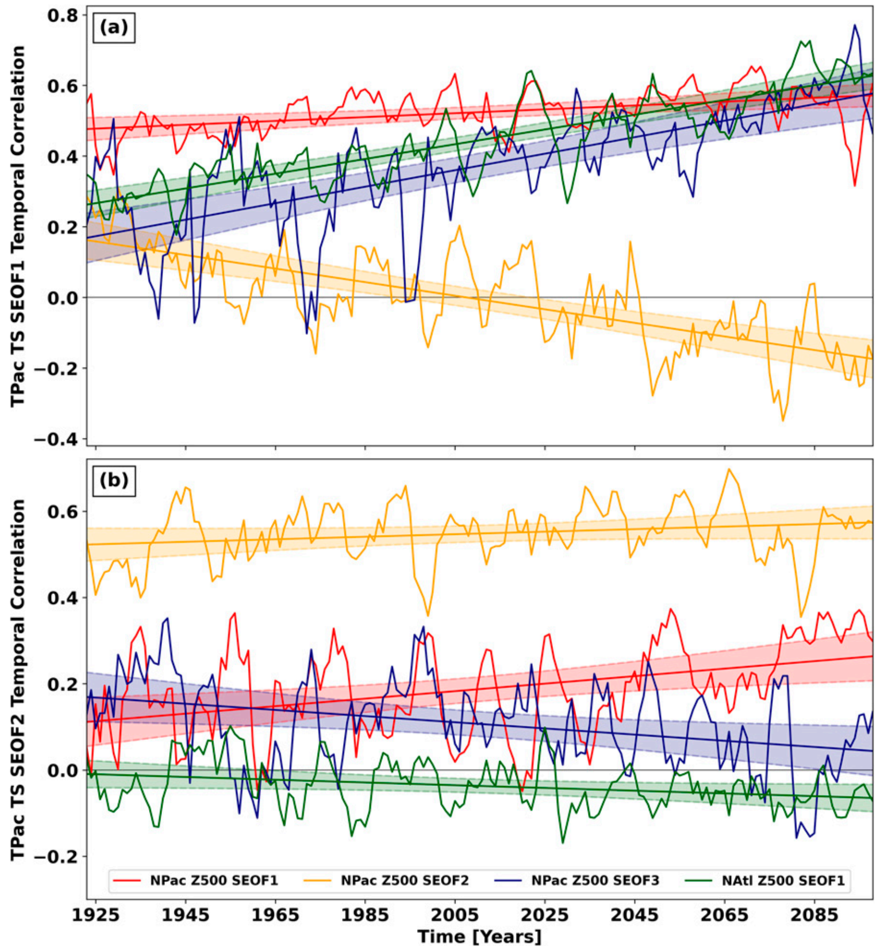

FIG. 4. Time-varying correlation coefficients between the SPC of each extratropical Z500 SEOF mode and the SPC of (a) TPac_TS_SEOF1 and (b) TPac_TS_SEOF2. The best-fit linear trend line and its associated 95% confidence interval (color shading) are also shown for each curve.

and is likely what explains the positive precipitation anomalies over the western United States, and in particular California, seen in Fig. 2d. This issue will be revisited and expanded upon further in the following section. For completeness, Fig. S6 shows the full set of correlation pairs for each mode considered.

b. Separating tropical and extratropical variability

Our results thus far indicate that tropical Pacific variability is projected to play an increasingly important role in driving patterns of atmospheric circulation variability over both the North Pacific and North Atlantic basins by the end of the twenty-first century. However, it is still unclear how much of the forced change in extratropical variability is due to tropical influences vs. intrinsic midlatitude dynamics. We now aim to separate the direct response of extratropical circulation variability to anthropogenic forcing from the indirect, tropically mediated response, referred to as “Pathway 1” and “Pathway 2,” respectively, in the schematic shown in Fig. 5. To accomplish this, we remove the linear correlations with TPac_TS_SPC1 and TPac_TS_SPC2 from the global Z500 field at each time step, and then apply SEOF analysis to the tropical-residual Z500 field using the same NPac and NAtl domains as before. The resulting tropical-residual Z500 SEOFs (hereafter, TRZ500 SEOFs) are largely devoid of tropical precipitation variability in both the early and late periods, as expected (Fig. 6). Nonetheless, they exhibit robust forced changes in their patterns and amplitudes, albeit less dramatic than those of the full Z500 SEOFs shown in Fig. 1. For example, NPac_TRZ500_SEOF1 shows an amplification of the maximum depth of the North Pacific trough by about 31% between the two periods (Figs. 6a,b; see Fig. S7 for significance of the Z500 fields). Comparing this to the deepening that occurs for NPac_Z500_SEOF1 (∼44%: Figs. 1a,b) indicates that the direct effect of external forcing is substantial relative to tropically mediated forcing (Pathway 2). On the other hand, NPac_TRZ500_SEOF2 shows very little change in its circulation or precipitation patterns between the early and late periods, indicating little sensitivity to the radiative effects associated with Pathway 1. However, when comparing the spatial characteristics of this mode with what is shown in Figs. 1c and 1d, it is evident that there are significant differences in its expression. This suggests that NPac_Z500_

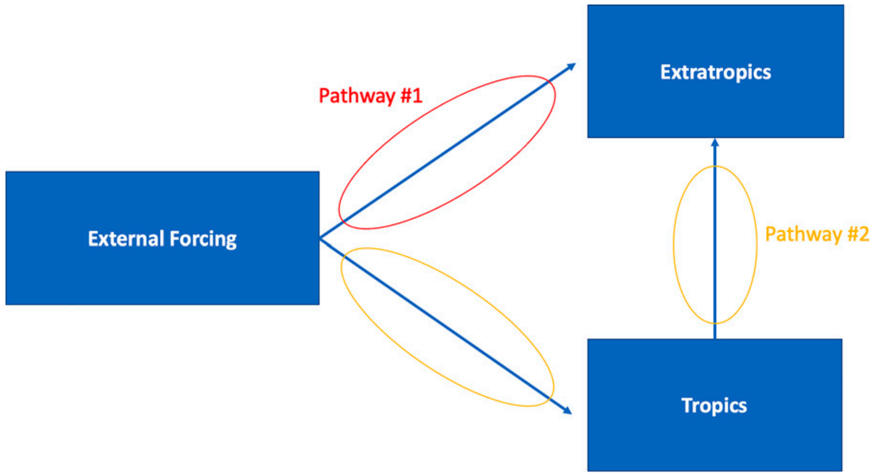

FIG. 5. Schematic diagram of the direct and indirect influences of external (i.e., anthropogenic) forcing on internal extratropical circulation variability. Pathway 1 represents the direct influence on intrinsic midlatitude dynamics. Pathway 2 depicts the indirect (tropically mediated) influence whereby external forcing acts directly on the tropics, which then drives teleconnections to the extratropics.

SEOF2 (NPO) depends strongly on tropical ocean variability for its existence.

NPac_TRZ500_SEOF3, which is associated with subtropical moisture transport, shows a modest increase in amplitude and a northeastward shift in the future, independent of tropical ENSO influence (Figs. 6e,f). In a box encompassing California, Oregon, and Washington, where the majority of the precipitation associated with NPac_TRZ500_SEOF3 is

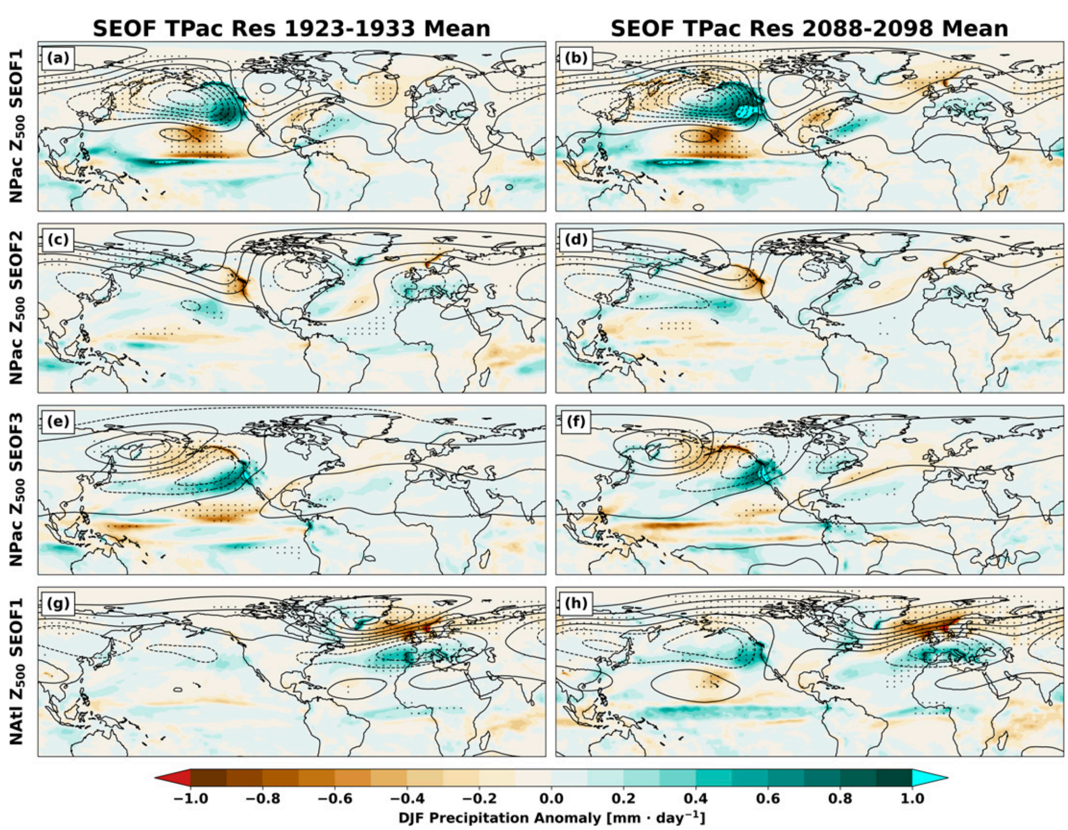

FIG. 6. As in Fig. 1 after removing the linear influence of the two leading SEOFs of tropical Pacific SST variability.

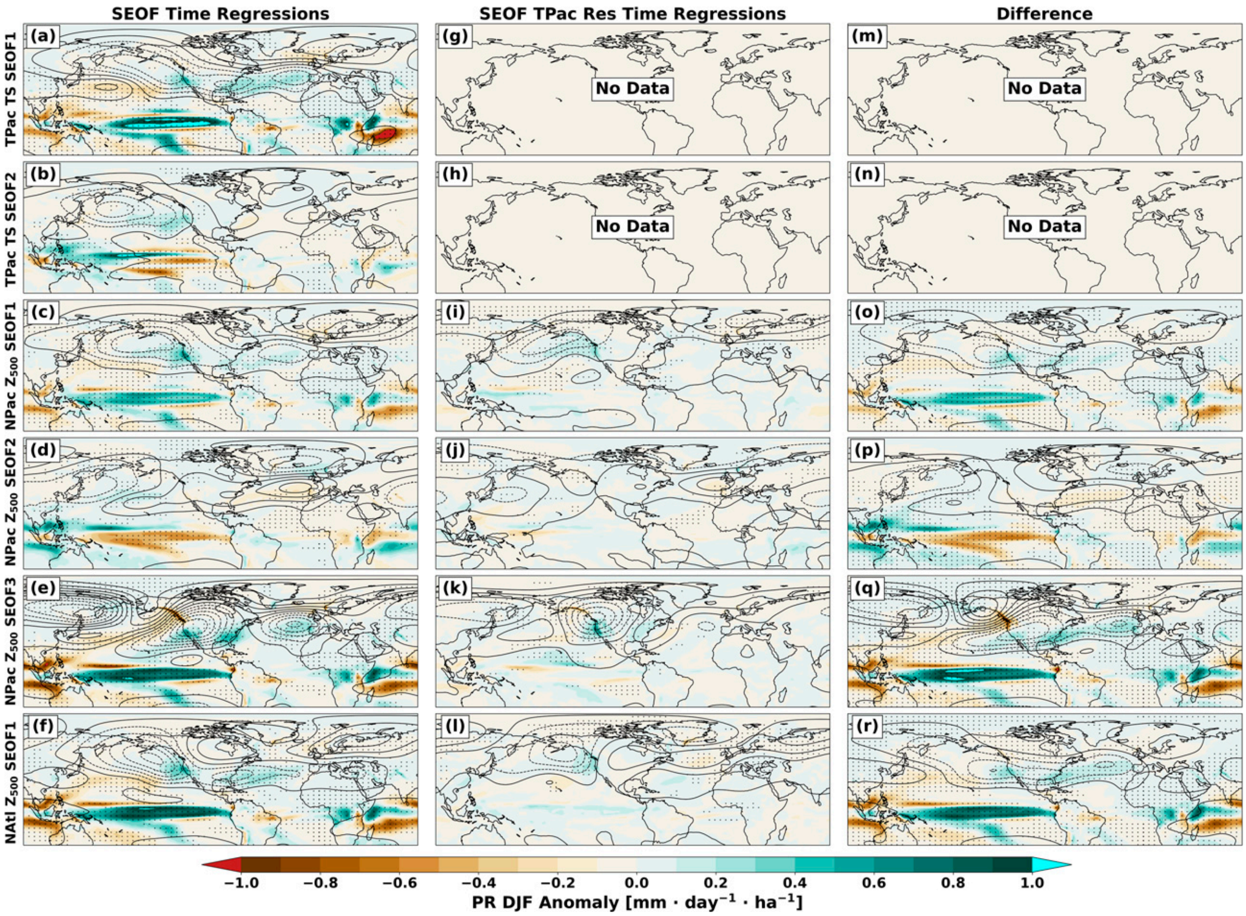

FIG. 7. Temporal linear regressions across the set of 176 time representations (years 1923–2098) of each SEOF mode (rows) based on (left) full fields and (center) tropical-residual fields. (right) The difference between the left and center columns. Precipitation is shown in color shading [mm day^{-1} ha^{-1}, where ha = hectoannum (or century)], and Z500 is contoured (contour interval = 4 m ha^{-1}; negative values dashed). Stippling indicates statistically significant values, determined when at least 50% of the years SEOF time slices have both statistically significant ($p \leq 0.1$) correlations across both the ensemble and time dimensions. Stippling in the difference field represents significance at $p \leq 0.1$ significance level according to a two-tailed t test.

focused, there is a ~40% increase in winter rainfall variability from the early to the late period. This suggests that in the future, even in years without strong ENSO activity, there exists a greater likelihood that this circulation mode could produce extremely wet or dry winters characterized by anomalous AR activity capable of rapidly exacerbating or ameliorating antecedent drought conditions (Dettinger 2013). Indeed, the western United States just experienced a poignant example of this type of atmospheric variability in the winter of 2017, when despite ENSO neutral conditions prevailing, California received record breaking winter precipitation driven by an anomalous number of ARs (Vahedifard et al. 2017; Vano et al. 2019; Patricola et al. 2020).

Future changes in NAtl_TRZ500_SEOF1 are relatively modest over the Atlantic sector, with a slight diminution in amplitude and eastward shift of its main centers of action, bringing enhanced precipitation variability to the eastern Mediterranean and western Scandinavia (Figs. 6g,h). Larger changes in this mode are evident over the North Pacific where they are reminiscent of the PNA, suggesting that external forcing will serve to better link the North Pacific and North Atlantic basins in a future warmer climate, independent of forced changes in ENSO, consistent with the findings of Drouard and Cassou (2019). However, most of the forced changes in NAtl_Z500_SEOF1 stem from resonant excitation by ENSO, as can be seen by comparing Figs. 1h and 6h.

Since the SEOF methodology yields a representation of unforced variability at each time step, we can concisely display the projected temporal changes in each unforced mode by linearly regressing the SEOFs across the time dimension (1923–2098). Figure 7 compares the temporal linear regression maps for the total (left column) and TPac Residual (center column) versions of the Z500 SEOF modes; analogous temporal regression maps for the two TPac_TS_SEOF modes based on total fields are shown in Figs. 7a and 7b. The right column of Fig. 7 shows the difference between the maps in the left and middle columns. These difference maps depict how forced trends in internal modes of TPac SST variability

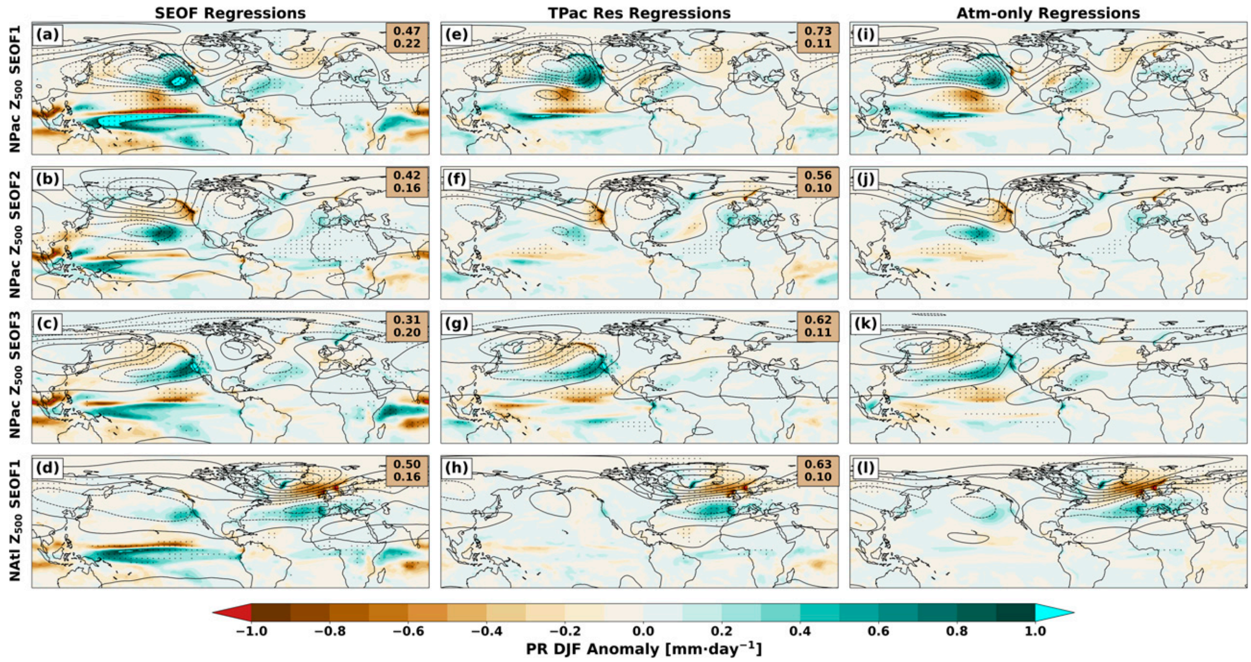

FIG. 8. DJF regression maps of precipitation (mm day^{-1}; color shading) and Z500 (contour interval = 10 m; negative values shown as dashed contours) for (a)–(c),(e)–(g),(i)–(k) the three leading SEOFs of North Pacific Z500 variability and (d),(h),(l) the leading SEOF of North Atlantic Z500 variability. Results based on the (left) CESM1-LE full and (center) tropical Pacific residual fields during 1923–33 are shown. (right) Analogous results based on the 2600-yr preindustrial atmosphere control simulation, formed by compositing 10 randomly sampled EOF calculations computed from 200-yr segments for consistency with the 10-yr averaging used for the SEOFs. See text for details. Stippling indicates that at least 7 out of 10 years had statistically significant regressions at the $p \leq 0.01$ significance level. Inset numbers show the pattern correlation and RMSE value (top and bottom numbers, respectively) of the precipitation regression field in the SEOF mode vs the corresponding EOF mode from the atmosphere-only control simulation in the right column.

modify forced trends in internal modes of Z500 variability. It is clear by comparing the columns of Fig. 7 that the relative contributions of direct external forcing (Pathway 1; center column) and tropically mediated forcing (Pathway 2; right column) depends on which SEOF mode is considered. NPac_Z500_SEOF1 shows roughly equal contributions from the two pathways, with some differences in their spatial patterns (cf. Figs. 7i,o). The tropically induced component (Fig. 7o) displays a strong spatial resemblance to the teleconnections associated with TPac_TS_SEOF1 (Fig. 7a), as expected based on the results shown in Fig. 4. Trends in NPac_Z500_SEOF2 are mainly due to the tropically mediated pathway over the North Pacific and to both pathways over the North Atlantic (Figs. 7d,j,p).

Interestingly, the modes that show the largest temporal trends are NPac_Z500_SEOF3 and NAtl_Z500_SEOF1 (Figs. 7e,f). Not coincidentally, these modes also exhibit the largest projected increases in linkages to TPac_TS_SEOF1 (recall Fig. 4a). While the tropically mediated pathway exerts a strong influence on the trends in these modes (Figs. 7q,r), intrinsic extratropical atmospheric dynamics also makes a substantial contribution (Figs. 7k,l). For example, the tropical-residual version of NPac_Z500_SEOF3 shows a prominent amplification of Z500 variability centered over British Columbia (maximum amplitudes around 14 m per century; Fig. 7k), while the tropically mediated component of this mode exhibits similar magnitude trends of opposite sign between Alaska and the western United States (Fig. 7q). It is also noteworthy that tropical influences explain approximately two-thirds of the NAO-like trends in this mode (cf. Figs. 7e,q).

As mentioned earlier, trends in Z500 variability associated with NAtl_Z500_SEOF1 are largest over the North Pacific and North America, areas outside the domain used to define the mode (Fig. 7f). This is due to the two pathways having opposing influences over the North Atlantic sector and constructive influences over the North Pacific region (Figs. 7l,r). The tropical Pacific influence on the trends in NAtl_Z500_SEOF1 (Fig. 7r) bears a strong resemblance to the trends associated with TPac_TS_SEOF1 (Fig. 7a), consistent with Fig. 4a. In summary, forced trends in all four modes of extratropical circulation variability and their associated impacts on precipitation are due to a combination of intrinsic atmospheric dynamics and tropically driven teleconnections. Forced changes in the preferred patterns of circulation variability driven by intrinsic atmospheric dynamics are likely to arise from forced changes in the circulation mean state, as demonstrated by Branstator and Selten (2009).

To verify our methodology for isolating intrinsic extratropical atmospheric dynamics, we leverage the 2600-yr atmosphere-only preindustrial control (atm-pictl) simulation described in section 2a. Figure 8 compares the full (left column) and TPac-

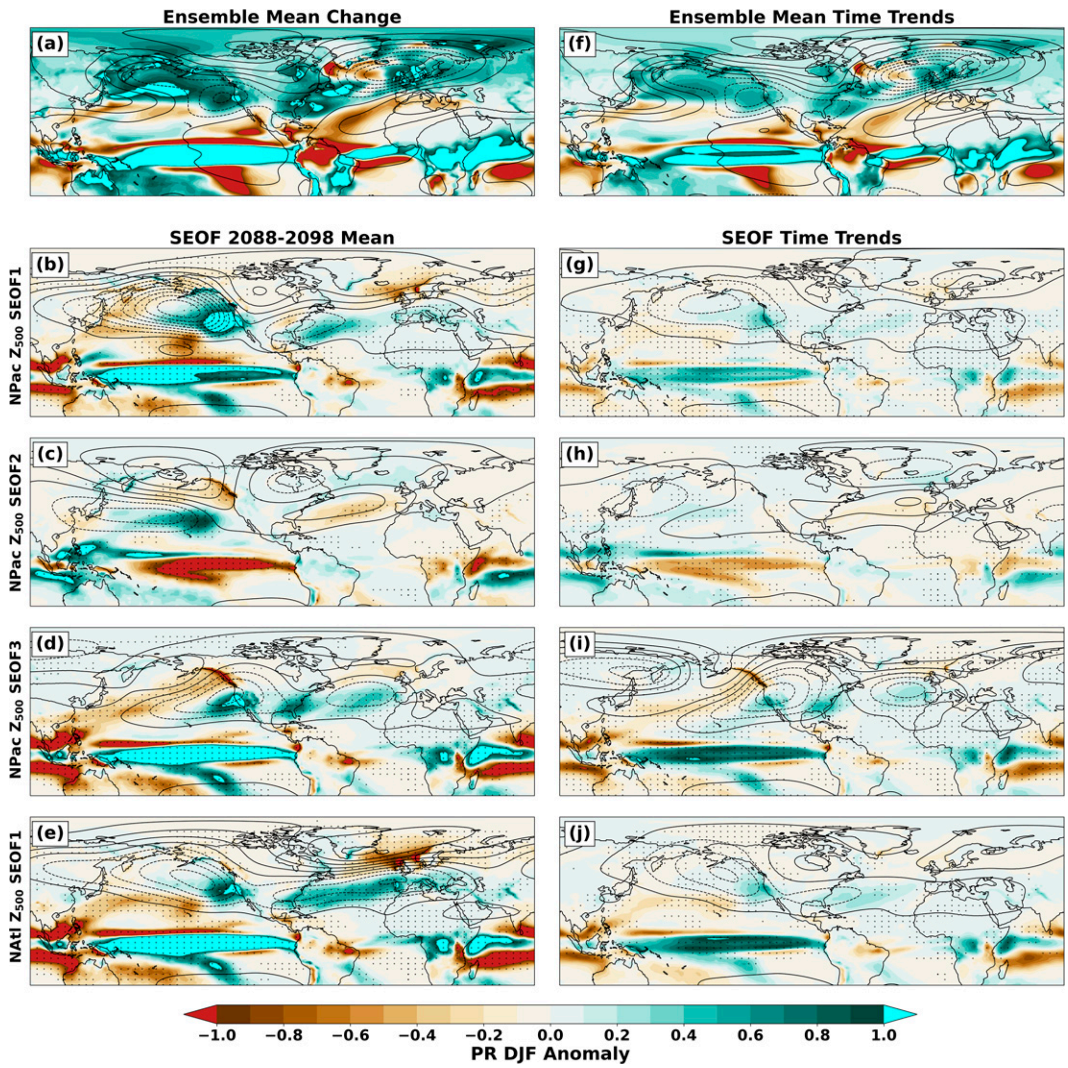

FIG. 9. Comparison of forced changes in the mean state vs forced changes in internal variability. (a) Ensemble-mean future (2085–100) minus past (1921–35) precipitation (color shading; mm day^{-1}) and Z500 (contour interval = 10 m, negative contours dashed). (b)–(e) Z500 SEOF modes averaged over the period 2088–98 (repeated from the right column of Fig. 1); color scale and contour interval are the same as in (a). (f) Ensemble-mean linear trends (1921–2100) of precipitation (color shading; mm day^{-1} century^{-1}) and Z500 (contour interval = 5 m century^{-1}; negative contours dashed). (g)–(j) Linear trends (1923–2098) of each Z500 SEOF mode (repeated from Figs. 7c–f); color scale and contour interval are the same as in (f).

residual (center column) Z500 SEOF modes during the first 10 years of the simulation with the atm-pictl EOFs (right column). Recall that the atm-pictl simulation has no interannual SST variability and therefore no ENSO of any kind. The TPac residual regression maps strongly mimic the atm-only results, indicating the residual regression methodology is effectively controlling for the effects of tropical SST variability on extratropical circulation and hydroclimate. In particular, the precipitation pattern correlations are considerably higher (and the spatial root-mean-squared errors (RMSE) are substantially lower) between the atm-pictl EOFs and TPac-residual SEOFs than they are between atm-pictl and the full Z500 SEOFs (see numbers in the panel insets to Figs. 8a–h), providing quantitative evidence for the efficacy of our methodology. For example, the precipitation pattern correlation for NPac_Z500_SEOF3 is 0.62 between the atm-pictl and the TPac-residual SEOF, and only 0.31 between the atm-pictl and the full SEOF, while the corresponding RMSE values are 0.20 and 0.11, respectively. These results are robust to sampling uncertainty as shown Fig. S8.

c. Comparing forced changes in internal variability versus forced changes in the mean state

In this section, we briefly compare forced changes in the internal modes of atmospheric circulation variability with forced changes in the mean state. Figure 9a shows the differences in ensemble-mean Z500 and precipitation between the periods 2085–100 minus 1921–35, indicative of forced changes in the mean state. Similar to other CMIP5 models, the CESM1-LE projects enhanced precipitation in the tropics and middle-to-high latitudes, and reduced precipitation in the subtropics, accompanied by decreased geopotential heights over the northern North Pacific and Atlantic, and increased heights at lower latitudes. These mean state circulation changes are similar in magnitude to the circulation anomalies associated with a one standard deviation departure of the internal modes of Z500 variability in the late twenty-first century (Figs. 9b–e). This indicates that the forced changes in mean circulation can easily be obscured by internal variability, consistent with previous studies (e.g., Deser et al. 2012a; Shepherd 2014; Deser et al. 2017a).

Next, we compare forced trends in the mean state with forced trends in the internal modes of variability over the period 1920–2100. It is evident that forced trends in the internal Z500 SEOF modes (Figs. 9g–j) are nonnegligible compared to forced trends in the Z500 mean state (Fig. 9f), especially for NPac_Z500_SEOF3 and Natl_Z500_SEOF1. Two conclusions regarding projected changes in extratropical circulation in the late twenty-first century can be drawn from these comparisons: 1) internal variability can obscure the mean state response to anthropogenic forcing; and 2) forced changes in the mean state are commensurate with forced changes in the leading modes of internal variability.

4. Summary and discussion

In this study, we have examined forced changes to unforced modes of extratropical atmospheric circulation variability over the North Pacific during winter as simulated by the 40-member CESM1 large ensemble over the period 1920–2100 using a novel "snapshot-EOF" methodology. This approach allows us to directly and succinctly quantify how anthropogenic emissions alter the spatial patterns and amplitudes of the leading modes of internal circulation variability and their associated impacts on precipitation over the course of the 20th and 21st centuries. We find that the internal modes of variability intensify and expand their spatial footprint in response to future climate change, with enhanced linkages to the tropics and the North Atlantic. Interestingly, it is North Pacific mode 3, which depicts the present-day "east Pacific pattern," that displays the largest forced changes, rather than modes 1 and 2 ("Pacific–North American" and "North Pacific Oscillation" patterns, respectively). Like many other models, CESM1 simulates future intensification of the two leading modes of tropical Pacific SST variability (canonical east Pacific and central Pacific Modoki ENSO) and an eastward shift in their associated tropical Pacific precipitation anomalies (Cai et al. 2014, 2020, 2021). These changes in ENSO activity contribute to the forced changes in the internal modes of extratropical circulation variability via tropically induced teleconnections. However, intrinsic midlatitude atmospheric dynamics independent of tropical influences also plays an important role. Finally, forced changes in amplitude of the leading internal modes of extratropical circulation variability are similar to those of the mean state, highlighting the need for an integrated approach to the study of anthropogenic climate change.

The preponderance of model evidence to date indicates that ENSO-related SST variability will increase in a future warmer climate (Cai et al. 2018; 2020, 2021) and display greater longitudinal variation in the location of associated tropical deep convection (Williams and Patricola 2018; Zhang et al. 2019), although mean state biases in thermal stratification may compromise the models' projected changes (Kohyama et al. 2018). For an expanded view of other ENSO indices (e.g., Niño-3.4, etc.) and metrics relating to this and other models/LEs the following references provide comprehensive summaries: Cai et al. (2018, 2020, 2021); Phillips et al. (2020); Dieppois et al. (2021); and Planton et al. (2021). While there are important exceptions to the projected increase in ENSO variability (e.g., Wengel et al. 2021), our results suggest that not only might the canonical ENSO teleconnections (e.g., the PNA) strengthen in the future, but presently variable/weak teleconnections may increase far more substantially. Indeed, the relationship between ENSO and NPac_Z500_SEOF3, which shows high interannual variability across the historical period, displays a consistently high correlation, on par with or even greater than that of the PNA by the end of the twenty-first century. This suggests that in the future NPac_Z500_SEOF3 will perhaps become an even more important component of the ENSO teleconnection than the PNA (Fig. 4a). Such historical intermittent excitation of NPac_Z500_SEOF3 by ENSO may be relevant for explaining the observed greatly amplified western U.S. hydroclimate response to the 1983 and 1998 extreme east Pacific El Niño events in observations.

Figures 1 and 6 show that NPac_Z500_SEOF1 (PNA) is associated with moisture transport to the western United States from the North Pacific, most likely in the form of extratropical cyclones (ETCs), while NPac_Z500_SEOF3 is associated with subtropical moisture transport, which is indicative of Pineapple Express–type AR activity. Given that these two modes are orthogonal, they represent independent moisture transport pathways that may be excited either independently or jointly. Thus, for example, considering the positive ENSO phase, the high variability shown in the historical period in the relationship between TPac_TS_SEOF1 and NPac_Z500_SEOF3 (Fig. 4a) suggests that some historical El Niño events may have been characterized by both of these moisture transport pathways, while others were not. Events such as these would likely have shown a high propensity of both ETC and AR activity over the winter period, and correspondingly, anomalously high rainfall, which could have led to severe and damaging flooding, particularly for the western United States.

Figure 4 further shows that in the future, the high interannual variability associated with NPac_Z500_SEOF3 during the historical period largely disappears toward the end of the century and that it is excited with an equally high likelihood as the PNA, suggesting a higher probability for damaging ENSO events in the future according to the CESM1-LE. El Niño events such as these would likely be more harmful than beneficial and pose serious risks to water control infrastructure and ecosystems (Corringham and Cayan 2019; O'Brien et al. 2019; Persad et al. 2020), especially in environments that have been previously impacted by wildfires (Cannon and DeGraff 2009), which is an ever-growing problem in the western United States (Westerling 2016; Williams et al. 2019). Similarly, in California, La Niña events would likely be characterized by deeper and more persistent drought conditions. Taken together, our results point to a future characterized by larger interannual precipitation variability, consistent with previous findings (Pendergrass et al. 2017; Swain et al. 2018). In addition, Fig. 4a also suggests that in both the historical and future climates, there is still substantial variability in both the PNA and EPP that is not explained by ENSO, and that it is not guaranteed that ENSO will excite either of those modes, either individually or simultaneously, in future extreme El Niño or La Niña events. Thus, the results from studying this LE imply that there will still be a relatively high probability for failed western U.S. hydroclimate responses to ENSO events, such as what happened in 2015/16 (Patricola et al. 2020).

From a prediction viewpoint, this study has several implications. First, due to the increasingly disproportionate influence ENSO will exert on global hydroclimate in the future, there may be more ability to forecast weather related impacts stemming from ENSO events (Figs. 2a,b). Given the greater and more consistent correlations between TPac_TS_SEOF1 and the extratropical Z500 SEOFs (except the NPO) in the future (Fig. 4a), this effectively translates into a more consistent hydroclimate response, especially when quantifying ENSO with an appropriate metric (Williams and Patricola 2018; Patricola et al. 2020; Nigam and Sengupta 2021). On the other hand, when controlling for variability originating in the tropics, only NPac_Z500_SEOF1 and NPac_Z500_SEOF3 show large and robust patterns of change (recall Figs. 6a,b,e,f, respectively). This indicates that these internal modes of variability amplify in a warming climate, potentially making seasonal-to-subseasonal prediction more challenging. For example, taken together, the externally forced changes in these two intrinsic atmospheric modes suggest that unpredictably wet (e.g., California winter 2017; Patricola et al. 2020) or dry (e.g., California winter 2013/14; Swain et al. 2014) winters will be more common in the western United States in a future warmer climate (Fig. 6). The increasingly unpredictable nature of wet/dry winters perhaps may be even more challenging from a water management perspective than an extreme El Niño/La Niña, since in the case of the latter, we can forecast and monitor ENSO development, and thus prepare. However, in the case of winters like 2014/17, they largely catch us by surprise, presenting immediate mitigation challenges that stress ecosystems and unprepared infrastructure to the point of failure (Vano et al. 2019; Persad et al. 2020). It is beyond the scope of this study to assess whether the unforced excitation of the NPac_Z500_SEOF1/3 modes were driving factors in the California winter of 2017; however, it is becoming increasingly clear that unforced variability plays an important and often disproportionate role in driving western U.S. precipitation (Dong et al. 2018; McKinnon and Deser 2021; Risser et al. 2021).

The results we have presented here implicitly assume that each of the modes of variability and their associated precipitation impacts are symmetric with respect to sign: That is, their patterns and amplitudes are equal and opposite between their negative and positive phases. Here, we shall briefly discuss the degree to which this assumption holds for the extratropical Z500 modes and the two tropical Pacific SST modes as documented in Figs. S9–S17. Overall, we find that this assumption holds reasonably well for the extratropical Z500 modes, especially in the early part of the twentieth century and to varying degrees in the latter part of the twenty-first century; however, it does not hold for the tropical Pacific SST modes.

The distributions of the extratropical Z500 SPCs based on kernel density estimates (O'Brien et al. 2016) show a high degree of symmetry in both the first 30 years and last 30 years of the 1921–2100 analysis period, while those for the TPac SST SPCs are asymmetric, consistent with previous studies (e.g., Dommenget et al. 2013; Fig. S9). Composite maps of the Z500, precipitation and temperature fields based on the upper (>90th percentile) and lower (<10th percentile) tails of the SPC distributions for each mode are shown in Figs. S10–S17 for both the early 30-yr period and the late 30-yr period. The sum of these composite maps, indicative of the degree of structural asymmetry between the positive and negative phases, is also shown for each mode and time period. As can be seen from Figs. S10 and S11, the asymmetric (nonlinear) component in the early period is generally small compared to the symmetric (linear) component of each Z500 mode (cf. magnitudes in the right column with those in the left and middle columns), although some localized differences are apparent. For example, the asymmetric component of NPac_Z500_SEOF1 (PNA) shows a cyclonic circulation feature that is highly reminiscent of the tropical Northern Hemisphere (TNH) pattern (Mo and Livezey 1986). While relatively small in amplitude, its proximity to the U.S. West Coast and impact on California precipitation highlights its potential importance to this region. The asymmetries in the other Z500 SEOFs are less pronounced in terms of their terrestrial precipitation impacts. More pronounced asymmetries are evident in the late period, although these nonlinearities are still generally weaker than the linear component of the extratropical Z500 modes (Figs. S12 and S13). These asymmetries in the Z500 modes are generally accompanied by asymmetries in tropical Pacific precipitation, suggestive of a tropical origin for the extratropical circulation nonlinearities. Further analysis is needed to assess the statistical significance of these asymmetries, and to probe their underlying dynamical mechanisms.

The two TPac SST modes show clear evidence of asymmetry in both time periods, as expected based on previous studies (Takahashi et al. 2011; Dommenget et al. 2013; Figs. S14–S17). A noteworthy feature is that the asymmetric component of TPac_TS_SEOF1 (Figs. S14c–S17c) bears a strong resemblance to the negative phase of TPac_TS_SEOF2 (Figs. S14e–S17e) in both time periods. Indeed, the nonlinear relationship between the two tropical modes shown in Fig. S3 indicates that it is virtually impossible to have a strong El Niño or La Niña without a similarly strong contribution from the negative phase of TPac_TS_SEOF2. On the other hand, TPac_TS_SEOF2 can express itself in either its positive or negative phase independent of TPac_TS_SEOF1, although this becomes less likely in the late period evidenced by the narrowing of the distribution where the TPac_TS_SEOF1 SPCs are near zero (Fig. S3). Further analysis is needed to assess how these asymmetries in the two TPac SST modes contribute to the asymmetries in the extratropical Z500 modes of variability discussed above.

Our results are based on a single model large ensemble, and thus call into question the extent to which the results are model dependent. Applying the snapshot EOF approach to other model LEs such as those in the Multi-Model Large Ensemble Archive (Deser et al. 2020) would provide additional insight into the robustness of future forced changes in the characteristics of internal modes of variability. Decomposing the forced changes into components related to ENSO versus intrinsic atmospheric dynamics would shed further light into the origins of model discrepancies, and possibly provide avenues for exploring possible emergent constraints (e.g., Simpson et al. 2021). Finally, there is scope for applying the framework used in this study to other regions and seasons.

Acknowledgments. We thank the members of NCAR's Climate Analysis Section, especially Isla R. Simpson, Adam S. Phillips, and John T. Fasullo, as well as Mark D. Risser of LBNL's EESA, for their helpful insights throughout the duration of this study. We also thank the editor and three anonymous reviewers for their insightful and constructive comments that greatly improved the quality of this manuscript. John. P. O'Brien was supported by the Climate and Large-Scale Dynamics Program in the Division of Atmospheric and Geospace Sciences at the National Science Foundation (NSF). This material is based upon work supported by the National Center for Atmospheric Research, which is a major facility sponsored by the NSF under Cooperative Agreement 1852977. The authors acknowledge high-performance computing support from Cheyenne (https://doi.org/10.5065/D6RX99HX) provided by the NCAR's Computational and Information Systems Laboratory, sponsored by the National Science Foundation. The authors know of no conflicts of interest with this publication.

Data availability statement. All data used in this study are openly available from the Earth System Grid (ESG; www.earthsystemgrid.org). Further information and ongoing experiments related to the CESM1-LE Project can be found online (https://www.cesm.ucar.edu/projects/community-projects/LENS/).

REFERENCES

AghaKouchak, A., D. Easterling, K. Hsu, S. Schubert, and S. Sorooshian, 2013: *Extremes in a Changing Climate: Detection, Analysis and Uncertainty*. Vol. 65, Springer, 426 pp., https://doi.org/10.1007/978-94-007-4479-0.

Ashok, K., S. K. Behera, S. A. Rao, H. Weng, and T. Yamagata, 2007: El Niño Modoki and its possible teleconnection. *J. Geophys. Res.*, **112**, C11007, https://doi.org/10.1029/2006JC003798.

Back, L. E., and C. S. Bretherton, 2009: On the relationship between SST gradients, boundary layer winds, and convergence over the tropical oceans. *J. Climate*, **22**, 4182–4196, https://doi.org/10.1175/2009JCLI2392.1.

Barnston, A. G., and R. E. Livezey, 1987: Classification, seasonality, and persistence of low-frequency atmospheric circulation patterns. *Mon. Wea. Rev.*, **115**, 1083–1126, https://doi.org/10.1175/1520-0493(1987)115<1083:CSAPOL>2.0.CO;2.

Bellenger, H., E. Guilyardi, J. Leloup, M. Lengaigne, and J. Vialard, 2014: ENSO representation in climate models: From CMIP3 to CMIP5. *Climate Dyn.*, **42**, 1999–2018, https://doi.org/10.1007/s00382-013-1783-z.

Benjamini, Y., and Y. Hochberg, 1995: Controlling the false discovery rate: A practical and powerful approach to multiple testing. *J. Roy. Stat. Soc.*, **57**, 289–300, https://doi.org/10.1111/j.2517-6161.1995.tb02031.x.

Beverley, J. D., M. Collins, F. H. Lambert, and R. Chadwick, 2021: Future changes to El Niño teleconnections over the North Pacific and North America. *J. Climate*, **34**, 6191–6205, https://doi.org/10.1175/JCLI-D-20-0877.1.

Bjerknes, J., 1969: Atmospheric teleconnections from the equatorial Pacific. *Mon. Wea. Rev.*, **97**, 163–172, https://doi.org/10.1175/1520-0493(1969)097<0163:ATFTEP>2.3.CO;2.

Bódai, T., G. Drótos, M. Herein, F. Lunkeit, and V. Lucarini, 2020: The forced response of the El Niño–Southern Oscillation–Indian Monsoon teleconnection in ensembles of Earth system models. *J. Climate*, **33**, 2163–2182, https://doi.org/10.1175/JCLI-D-19-0341.1.

Brandefelt, J., and H. Körnich, 2008: Northern Hemisphere stationary waves in future climate projections. *J. Climate*, **21**, 6341–6353, https://doi.org/10.1175/2008JCLI2373.1.

Branstator, G., and F. Selten, 2009: "Modes of variability" and climate change. *J. Climate*, **22**, 2639–2658, https://doi.org/10.1175/2008JCLI2517.1.

——, and H. Teng, 2010: Two limits of initial-value decadal predictability in a CGCM. *J. Climate*, **23**, 6292–6311, https://doi.org/10.1175/2010JCLI3678.1.

——, and ——, 2017: Tropospheric waveguide teleconnections and their seasonality. *J. Atmos. Sci.*, **74**, 1513–1532, https://doi.org/10.1175/JAS-D-16-0305.1.

Cai, W., and Coauthors, 2014: Increasing frequency of extreme El Niño events due to greenhouse warming. *Nat. Climate Change*, **4**, 111–116, https://doi.org/10.1038/nclimate2100.

——, and Coauthors, 2018: Increased variability of eastern Pacific El Niño under greenhouse warming. *Nature*, **564**, 201–206, https://doi.org/10.1038/s41586-018-0776-9.

——, A. Santoso, G. Wang, L. Wu, M. Collins, M. Lengaigne, S. Power, and A. Timmermann, 2020: ENSO response to greenhouse forcing. *El Niño Southern Oscillation in a Changing Climate*, M. J. McPhaden, A. Santoso, and W. Cai, Eds., John Wiley and Sons, 289–307, https://doi.org/10.1002/9781119548164.ch13.

——, and Coauthors, 2021: Changing El Niño–Southern Oscillation in a warming climate. *Nat. Rev. Earth Environ.*, **2**, 628–644, https://doi.org/10.1038/s43017-021-00199-z.

Cannon, S. H., and J. DeGraff, 2009: The increasing wildfire and post-fire debris-flow threat in Western USA, and implications for consequences of climate change. *Landslides—Disaster Risk Reduction*, K. Sassa and P. Canuti, Eds., Springer, 177–190, https://doi.org/10.1007/978-3-540-69970-5_9.

Capotondi, A., and Coauthors, 2015: Understanding ENSO diversity. *Bull. Amer. Meteor. Soc.*, **96**, 921–938, https://doi.org/10.1175/BAMS-D-13-00117.1.

——, A. T. Wittenberg, J.-S. Kug, K. Takahashi, and M. J. McPhaden, 2020: ENSO diversity. *El Niño Southern*

Oscillation in a Changing Climate, M. J. McPhaden, A. Santoso, and W. Cai, Eds., John Wiley and Sons, 65–86, https://doi.org/10.1002/9781119548164.ch4.

Chen, Z., B. Gan, L. Wu, and F. Jia, 2018: Pacific-North American teleconnection and North Pacific Oscillation: Historical simulation and future projection in CMIP5 models. *Climate Dyn.*, **50**, 4379–4403, https://doi.org/10.1007/s00382-017-3881-9.

Collins, M., and Coauthors, 2010: The impact of global warming on the tropical Pacific Ocean and El Niño. *Nat. Geosci.*, **3**, 391–397, https://doi.org/10.1038/ngeo868.

Corringham, T. W., and D. R. Cayan, 2019: The effect of El Niño on flood damages in the western United States. *Wea. Climate Soc.*, **11**, 489–504, https://doi.org/10.1175/WCAS-D-18-0071.1.

DelSole, T., and M. K. Tippett, 2018: Predictability in a changing climate. *Climate Dyn.*, **51**, 531–545, https://doi.org/10.1007/s00382-017-3939-8.

Deser, C., 2020: Certain uncertainty: The role of internal climate variability in projections of regional climate change and risk management. *Earth's Future*, **8**, e2020EF001854, https://doi.org/10.1029/2020EF001854.

——, A. Phillips, V. Bourdette, and H. Teng, 2012a: Uncertainty in climate change projections: The role of internal variability. *Climate Dyn.*, **38**, 527–546, https://doi.org/10.1007/s00382-010-0977-x.

——, R. Knutti, S. Solomon, and A. S. Phillips, 2012b: Communication of the role of natural variability in future North American climate. *Nat. Climate Change*, **2**, 775–779, https://doi.org/10.1038/nclimate1562.

——, J. W. Hurrell, and A. S. Phillips, 2017a: The role of the North Atlantic Oscillation in European climate projections. *Climate Dyn.*, **49**, 3141–3157, https://doi.org/10.1007/s00382-016-3502-z.

——, I. R. Simpson, K. A. McKinnon, and A. S. Phillips, 2017b: The Northern Hemisphere extratropical atmospheric circulation response to ENSO: How well do we know it and how do we evaluate models accordingly? *J. Climate*, **30**, 5059–5082, https://doi.org/10.1175/JCLI-D-16-0844.1.

——, ——, A. S. Phillips, and K. A. McKinnon, 2018: How well do we know ENSO's climate impacts over North America, and how do we evaluate models accordingly? *J. Climate*, **31**, 4991–5014, https://doi.org/10.1175/JCLI-D-17-0783.1.

——, and Coauthors, 2020: Insights from Earth system model initial-condition large ensembles and future prospects. *Nat. Climate Change*, **10**, 277–286, https://doi.org/10.1038/s41558-020-0731-2.

Dettinger, M. D., 2013: Atmospheric rivers as drought busters on the U.S. West Coast. *J. Hydrometeor.*, **14**, 1721–1732, https://doi.org/10.1175/JHM-D-13-02.1.

DeWeaver, E., and S. Nigam, 2004: On the forcing of ENSO teleconnections by anomalous heating and cooling. *J. Climate*, **17**, 3225–3235, https://doi.org/10.1175/1520-0442(2004)017<3225:OTFOET>2.0.CO;2.

Diaz, H. F., M. P. Hoerling, and J. K. Eischeid, 2001: ENSO variability, teleconnections and climate change. *Int. J. Climatol.*, **21**, 1845–1862, https://doi.org/10.1002/joc.631.

Dieppois, B., A. Capotondi, B. Pohl, K. P. Chun, P.-A. Monerie, and J. Eden, 2021: ENSO diversity shows robust decadal variations that must be captured for accurate future projections. *Commun. Earth Environ.*, **2**, 212, https://doi.org/10.1038/s43247-021-00285-6.

Dommenget, D., T. Bayr, and C. Frauen, 2013: Analysis of the non-linearity in the pattern and time evolution of El Niño Southern Oscillation. *Climate Dyn.*, **40**, 2825–2847, https://doi.org/10.1007/s00382-012-1475-0.

Dong, L., L. R. Leung, F. Song, and J. Lu, 2018: Roles of SST versus internal atmospheric variability in winter extreme precipitation variability along the U.S. West Coast. *J. Climate*, **31**, 8039–8058, https://doi.org/10.1175/JCLI-D-18-0062.1.

Drótos, G., T. Bódai, and T. Tél, 2015: Probabilistic concepts in a changing climate: A snapshot attractor picture. *J. Climate*, **28**, 3275–3288, https://doi.org/10.1175/JCLI-D-14-00459.1.

Drouard, M., and C. Cassou, 2019: A modeling- and process-oriented study to investigate the projected change of ENSO-forced wintertime teleconnectivity in a warmer world. *J. Climate*, **32**, 8047–8068, https://doi.org/10.1175/JCLI-D-18-0803.1.

Fasullo, J. T., A. S. Phillips, and C. Deser, 2020: Evaluation of leading modes of climate variability in the CMIP archives. *J. Climate*, **33**, 5527–5545, https://doi.org/10.1175/JCLI-D-19-1024.1.

Feldstein, S. B., 2000: The timescale, power spectra, and climate noise properties of teleconnection patterns. *J. Climate*, **13**, 4430–4440, https://doi.org/10.1175/1520-0442(2000)013<4430:TTPSAC>2.0.CO;2.

——, and C. L. E. Franzke, 2017: Atmospheric teleconnection patterns. *Nonlinear and Stochastic Climate Dynamics*, C. L. E. Franzke and T. J. OKane, Eds., Cambridge University Press, 54–104, https://doi.org/10.1017/9781316339251.004.

Fereday, D. R., R. Chadwick, J. R. Knight, and A. A. Scaife, 2020: Tropical rainfall linked to stronger future ENSO-NAO teleconnection in CMIP5 models. *Geophys. Res. Lett.*, **47**, e2020GL088664, https://doi.org/10.1029/2020GL088664.

Frauen, C., and D. Dommenget, 2010: El Niño and La Niña amplitude asymmetry caused by atmospheric feedbacks. *Geophys. Res. Lett.*, **37**, L18801, https://doi.org/10.1029/2010GL044444.

Gershunov, A., and Coauthors, 2019: Precipitation regime change in western North America: The role of atmospheric rivers. *Sci. Rep.*, **9**, 9944, https://doi.org/10.1038/s41598-019-46169-w.

Gillett, N., H.-F. Graf, and T. Osborn, 2003: Climate change and the North Atlantic oscillation. *The North Atlantic Oscillation: Climatic Significance and Environmental Impact,* J. W. Hurrell et al., Eds., Vol. 134, Amer. Geophys. Union, 193–209, https://doi.org/10.1029/134GM09.

Guo, R., C. Deser, L. Terray, and F. Lehner, 2019: Human influence on winter precipitation trends (1921–2015) over North America and Eurasia revealed by dynamical adjustment. *Geophys. Res. Lett.*, **46**, 3426–3434, https://doi.org/10.1029/2018GL081316.

Haszpra, T., M. Herein, and T. Bódai, 2020a: Investigating ENSO and its teleconnections under climate change in an ensemble view—A new perspective. *Earth Syst. Dyn.*, **11**, 267–280, https://doi.org/10.5194/esd-11-267-2020.

——, D. Topál, and M. Herein, 2020b: On the time evolution of the Arctic Oscillation and related wintertime phenomena under different forcing scenarios in an ensemble approach. *J. Climate*, **33**, 3107–3124, https://doi.org/10.1175/JCLI-D-19-0004.1.

Hawkins, E., and R. Sutton, 2009: The potential to narrow uncertainty in regional climate predictions. *Bull. Amer. Meteor. Soc.*, **90**, 1095–1108, https://doi.org/10.1175/2009BAMS2607.1.

He, L., X. Hao, and T. Han, 2021: The asymmetric impacts of ENSO Modoki on boreal winter climate over the Pacific and its rim. *Climate Dyn.*, **56**, 29–44, https://doi.org/10.1007/s00382-020-05395-z.

Herein, M., J. Márfy, G. Drótos, and T. Tél, 2016: Probabilistic concepts in intermediate-complexity climate models: A snapshot attractor picture. *J. Climate*, **29**, 259–272, https://doi.org/10.1175/JCLI-D-15-0353.1.

——, G. Drótos, T. Haszpra, J. Márfy, and T. Tél, 2017: The theory of parallel climate realizations as a new framework for teleconnection analysis. *Sci. Rep.*, **7**, 44529, https://doi.org/10.1038/srep44529.

Hoerling, M. P., and M. Ting, 1994: Organization of extratropical transients during El Niño. *J. Climate*, **7**, 745–766, https://doi.org/10.1175/1520-0442(1994)007<0745:OOETDE>2.0.CO;2.

——, A. Kumar, and M. Zhong, 1997: El Niño, La Niña, and the nonlinearity of their teleconnections. *J. Climate*, **10**, 1769–1786, https://doi.org/10.1175/1520-0442(1997)010<1769:ENOLNA>2.0.CO;2.

Huang, P., and S.-P. Xie, 2015: Mechanisms of change in ENSO-induced tropical Pacific rainfall variability in a warming climate. *Nat. Geosci.*, **8**, 922–926, https://doi.org/10.1038/ngeo2571.

Huang, Y., H.-L. Ren, R. Chadwick, Z. Cheng, and Q. Chen, 2018: Diagnosing changes of winter NAO in response to different climate forcings in a set of atmosphere-only timeslice experiments. *Atmosphere*, **9**, 10, https://doi.org/10.3390/atmos9010010.

Hurrell, J. W., 1995: Decadal trends in the North Atlantic Oscillation: Regional temperatures and precipitation. *Science*, **269**, 676–679, https://doi.org/10.1126/science.269.5224.676.

——, Y. Kushnir, G. Ottersen, and M. Visbeck, 2003: An overview of the North Atlantic Oscillation. *The North Atlantic Oscillation: Climatic Significance and Environmental Impact*, J. W. Hurrell et al., Eds., Vol. 134, Amer. Geophys. Union, 1–35, https://doi.org/10.1029/134GM01.

IPCC, 2007: *Climate Change 2007: The Physical Science Basis*. Cambridge University Press, 996 pp.

IPCC, 2013: *Climate Change 2013: The Physical Science Basis*. Cambridge University Press, 1535 pp., https://doi.org/10.1017/CBO9781107415324.

——, 2021: *Climate Change 2021: The Physical Science Basis*. Cambridge University Press, in press, https://doi.org/10.1017/9781009157896.

Kao, H.-Y., and J.-Y. Yu, 2009: Contrasting eastern-Pacific and central-Pacific types of ENSO. *J. Climate*, **22**, 615–632, https://doi.org/10.1175/2008JCLI2309.1.

Kay, J. E., and Coauthors, 2015: The Community Earth System Model (CESM) large ensemble project: A community resource for studying climate change in the presence of internal climate variability. *Bull. Amer. Meteor. Soc.*, **96**, 1333–1349, https://doi.org/10.1175/BAMS-D-13-00255.1.

Kohyama, T., D. L. Hartmann, and D. S. Battisti, 2018: Weakening of nonlinear ENSO under global warming. *Geophys. Res. Lett.*, **45**, 8557–8567, https://doi.org/10.1029/2018GL079085.

Leathers, D. J., B. Yarnal, and M. A. Palecki, 1991: The Pacific/North American teleconnection pattern and United States climate. Part I: Regional temperature and precipitation associations. *J. Climate*, **4**, 517–528, https://doi.org/10.1175/1520-0442(1991)004<0517:TPATPA>2.0.CO;2.

Lindzen, R. S., and S. Nigam, 1987: On the role of sea surface temperature gradients in forcing low-level winds and convergence in the tropics. *J. Atmos. Sci.*, **44**, 2418–2436, https://doi.org/10.1175/1520-0469(1987)044<2418:OTROSS>2.0.CO;2.

Linkin, M. E., and S. Nigam, 2008: The North Pacific Oscillation–West Pacific teleconnection pattern: Mature-phase structure and winter impacts. *J. Climate*, **21**, 1979–1997, https://doi.org/10.1175/2007JCLI2048.1.

Lorenz, E. N., 1963: Deterministic nonperiodic flow. *J. Atmos. Sci.*, **20**, 130–141, https://doi.org/10.1175/1520-0469(1963)020<0130:DNF>2.0.CO;2.

Maher, N., D. Matei, S. Milinski, and J. Marotzke, 2018: ENSO change in climate projections: Forced response or internal variability? *Geophys. Res. Lett.*, **45**, 11 390–11 398, https://doi.org/10.1029/2018GL079764.

Mankin, J. S., F. Lehner, S. Coats, and K. A. McKinnon, 2020: The value of initial condition large ensembles to robust adaptation decision-making. *Earth's Future*, **8**, e2012EF001610, https://doi.org/10.1029/2020EF001610.

Mann, M. E., S. Rahmstorf, K. Kornhuber, B. A. Steinman, S. K. Miller, and D. Coumou, 2017: Influence of anthropogenic climate change on planetary wave resonance and extreme weather events. *Sci. Rep.*, **7**, 45242, https://doi.org/10.1038/srep45242.

McKenna, C. M., and A. C. Maycock, 2021: Sources of uncertainty in multimodel large ensemble projections of the winter North Atlantic Oscillation. *Geophys. Res. Lett.*, **48**, e2021GL093258, https://doi.org/10.1029/2021GL093258.

McKinnon, K. A., and C. Deser, 2021: The inherent uncertainty of precipitation variability, trends, and extremes due to internal variability, with implications for western U.S. water resources. *J. Climate*, **34**, 9605–9622, https://doi.org/10.1175/JCLI-D-21-0251.1.

Michel, C., C. Li, I. R. Simpson, I. Bethke, M. P. King, and S. Sobolowski, 2020: The change in the ENSO teleconnection under a low global warming scenario and the uncertainty due to internal variability. *J. Climate*, **33**, 4871–4889, https://doi.org/10.1175/JCLI-D-19-0730.1.

Milinski, S., N. Maher, and D. Olonscheck, 2020: How large does a large ensemble need to be? *Earth Syst. Dyn.*, **11**, 885–901, https://doi.org/10.5194/esd-11-885-2020.

Milly, P. C. D., J. Betancourt, M. Falkenmark, R. M. Hirsch, Z. W. Kundzewicz, D. P. Lettenmaier, and R. J. Stouffer, 2008: Stationarity is dead: Whither water management? *Science*, **319**, 573–574, https://doi.org/10.1126/science.1151915.

Mo, K. C., and R. E. Livezey, 1986: Tropical-extratropical geopotential height teleconnections during the Northern Hemisphere winter. *Mon. Wea. Rev.*, **114**, 2488–2515, https://doi.org/10.1175/1520-0493(1986)114<2488:TEGHTD>2.0.CO;2.

Müller, W. A., and E. Roeckner, 2008: ENSO teleconnections in projections of future climate in ECHAM5/MPI-OM. *Climate Dyn.*, **31**, 533–549, https://doi.org/10.1007/s00382-007-0357-3.

Nigam, S., and A. Sengupta, 2021: The full extent of El Niño's precipitation influence on the United States and the Americas: The suboptimality of the Niño-3.4 SST index. *Geophys. Res. Lett.*, **48**, e2020GL091447, https://doi.org/10.1029/2020GL091447.

North, G. R., T. L. Bell, R. F. Cahalan, and F. J. Moeng, 1982: Sampling errors in the estimation of empirical orthogonal functions. *Mon. Wea. Rev.*, **110**, 699–706, https://doi.org/10.1175/1520-0493(1982)110<0699:SEITEO>2.0.CO;2.

O'Brien, J. P., T. A. O'Brien, C. M. Patricola, and S.-Y. Simon Wang, 2019: Metrics for understanding large-scale controls of multivariate temperature and precipitation variability. *Climate Dyn.*, **53**, 3805–3823, https://doi.org/10.1007/s00382-019-04749-6.

O'Brien, T. A., K. Kashinath, N. R. Cavanaugh, W. D. Collins, and J. P. O'Brien, 2016: A fast and objective multidimensional kernel density estimation method: FastKDE. *Comput. Stat. Data Anal.*, **101**, 148–160, https://doi.org/10.1016/j.csda.2016.02.014.

——, and Coauthors, 2020: Detection uncertainty matters for understanding atmospheric rivers. *Bull. Amer. Meteor. Soc.*, **101**, E790–E796, https://doi.org/10.1175/BAMS-D-19-0348.1.

——, and Coauthors, 2022: Increases in future AR count and size: Overview of the ARTMIP Tier 2 CMIP5/6 experiment. *J. Geophys. Res. Atmos.*, **127**, e2021JD036013, https://doi.org/10.1029/2021JD036013.

Patricola, C. M., J. P. O'Brien, M. D. Risser, A. M. Rhoades, T. A. O'Brien, P. A. Ullrich, D. A. Stone, and W. D. Collins, 2020: Maximizing ENSO as a source of western U.S. hydroclimate predictability. *Climate Dyn.*, **54**, 351–372, https://doi.org/10.1007/s00382-019-05004-8.

Payne, A. E., and Coauthors, 2020: Responses and impacts of atmospheric rivers to climate change. *Nat. Rev. Earth Environ.*, **1**, 143–157, https://doi.org/10.1038/s43017-020-0030-5.

Pendergrass, A. G., R. Knutti, F. Lehner, C. Deser, and B. M. Sanderson, 2017: Precipitation variability increases in a warmer climate. *Sci. Rep.*, **7**, 17966, https://doi.org/10.1038/s41598-017-17966-y.

Persad, G. G., D. L. Swain, C. Kouba, and J. P. Ortiz-Partida, 2020: Inter-model agreement on projected shifts in California hydroclimate characteristics critical to water management. *Climatic Change*, **162**, 1493–1513, https://doi.org/10.1007/s10584-020-02882-4.

Phillips, A. S., C. Deser, J. Fasullo, D. P. Schneider, and I. R. Simpson, 2020: Assessing climate variability and change in model large ensembles: A user's guide to the "Climate Variability Diagnostics Package for Large Ensembles" version 1.0. NCAR, 53 pp., https://doi.org/10.5065/h7c7-f961.

Planton, Y. Y., and Coauthors, 2021: Evaluating climate models with the CLIVAR 2020 ENSO metrics package. *Bull. Amer. Meteor. Soc.*, **102**, E193–E217, https://doi.org/10.1175/BAMS-D-19-0337.1.

Power, S., F. Delage, C. Chung, G. Kociuba, and K. Keay, 2013: Robust twenty-first-century projections of El Niño and related precipitation variability. *Nature*, **502**, 541–545, https://doi.org/10.1038/nature12580.

Rhoades, A. M., M. D. Risser, D. A. Stone, M. F. Wehner, and A. D. Jones, 2021: Implications of warming on western United States landfalling atmospheric rivers and their flood damages. *Wea. Climate Extreme*, **32**, 100326, https://doi.org/10.1016/j.wace.2021.100326.

Riahi, K., and Coauthors, 2011: RCP 8.5—A scenario of comparatively high greenhouse gas emissions. *Climatic Change*, **109**, 33, https://doi.org/10.1007/s10584-011-0149-y.

Risser, M. D., M. F. Wehner, J. P. O'Brien, C. M. Patricola, T. A. O'Brien, W. D. Collins, C. J. Paciorek, and H. Huang, 2021: Quantifying the influence of natural climate variability on in situ measurements of seasonal total and extreme daily precipitation. *Climate Dyn.*, **56**, 3205–3230, https://doi.org/10.1007/s00382-021-05638-7.

Ropelewski, C. F., and M. S. Halpert, 1987: Global and regional scale precipitation patterns associated with the El Niño/Southern Oscillation. *Mon. Wea. Rev.*, **115**, 1606–1626, https://doi.org/10.1175/1520-0493(1987)115<1606:GARSPP>2.0.CO;2.

Rutz, J. J., and Coauthors, 2019: The Atmospheric River Tracking Method Intercomparison Project (ARTMIP): Quantifying uncertainties in atmospheric river climatology. *J. Geophys. Res. Atmos.*, **124**, 13 777–13 802, https://doi.org/10.1029/2019JD030936.

Sarhadi, A., M. C. Ausín, M. P. Wiper, D. Touma, and N. S. Diffenbaugh, 2018: Multidimensional risk in a nonstationary climate: Joint probability of increasingly severe warm and dry conditions. *Sci. Adv.*, **4**, eaau3487, https://doi.org/10.1126/sciadv.aau3487.

Shepherd, T. G., 2014: Atmospheric circulation as a source of uncertainty in climate change projections. *Nat. Geosci.*, **7**, 703–708, https://doi.org/10.1038/ngeo2253.

Simpson, I. R., T. A. Shaw, and R. Seager, 2014: A diagnosis of the seasonally and longitudinally varying midlatitude circulation response to global warming. *J. Atmos. Sci.*, **71**, 2489–2515, https://doi.org/10.1175/JAS-D-13-0325.1.

——, K. A. McKinnon, F. V. Davenport, M. Tingley, F. Lehner, A. Al Fahad, and D. Chen, 2021: Emergent constraints on the large-scale atmospheric circulation and regional hydroclimate: Do they still work in CMIP6 and how much can they actually constrain the future? *J. Climate*, **34**, 6355–6377, https://doi.org/10.1175/JCLI-D-21-0055.1.

Stan, C., D. M. Straus, J. S. Frederiksen, H. Lin, E. D. Maloney, and C. Schumacher, 2017: Review of tropical-extratropical teleconnections on intraseasonal time scales. *Rev. Geophys.*, **55**, 902–937, https://doi.org/10.1002/2016RG000538.

Stevenson, S., A. T. Wittenberg, J. Fasullo, S. Coats, and B. Otto-Bliesner, 2021: Understanding diverse model projections of future extreme El Niño. *J. Climate*, **34**, 449–464, https://doi.org/10.1175/JCLI-D-19-0969.1.

Swain, D. L., M. Tsiang, M. Haugen, D. Singh, A. Charland, B. Rajaratnam, and N. S. Diffenbaugh, 2014: The extraordinary California drought of 2013/2014: Character, context, and the role of climate change [in "Explaining Extremes of 2013 from a Climate Perspective"]. *Bull. Amer. Meteor. Soc.*, **95** (9), S3–S7, https://doi.org/10.1175/1520-0477-95.9.S1.1.

——, B. Langenbrunner, J. D. Neelin, and A. Hall, 2018: Increasing precipitation volatility in twenty-first-century California. *Nat. Climate Change*, **8**, 427–433, https://doi.org/10.1038/s41558-018-0140-y.

Takahashi, K., A. Montecinos, K. Goubanova, and B. Dewitte, 2011: ENSO regimes: Reinterpreting the canonical and Modoki El Niño. *Geophys. Res. Lett.*, **38**, L10704, https://doi.org/10.1029/2011GL047364.

Tebaldi, C., and R. Knutti, 2007: The use of the multi-model ensemble in probabilistic climate projections. *Philos. Trans. Roy. Soc.*, **365**, 2053–2075, https://doi.org/10.1098/rsta.2007.2076.

Teng, H., G. Branstator, A. B. Tawfik, and P. Callaghan, 2019: Circumglobal response to prescribed soil moisture over North America. *J. Climate*, **32**, 4525–4545, https://doi.org/10.1175/JCLI-D-18-0823.1.

Thomson, S. I., and G. K. Vallis, 2018: Atmospheric response to SST anomalies. Part I: Background-state dependence, teleconnections, and local effects in winter. *J. Atmos. Sci.*, **75**, 4107–4124, https://doi.org/10.1175/JAS-D-17-0297.1.

Vahedifard, F., A. AghaKouchak, E. Ragno, S. Shahrokhabadi, and I. Mallakpour, 2017: Lessons from the Oroville dam. *Science*, **355**, 1139–1140, https://doi.org/10.1126/science.aan0171.

Vano, J. A., K. Miller, M. D. Dettinger, R. Cifelli, D. Curtis, A. Dufour, J. R. Olsen, and A. M. Wilson, 2019: Hydroclimatic extremes as challenges for the water management community: Lessons from Oroville Dam and Hurricane Harvey. *Bull. Amer. Meteor. Soc.*, **100**, S9–S14, https://doi.org/10.1175/BAMS-D-18-0219.1.

van Vuuren, D. P., and Coauthors, 2011: The representative concentration pathways: An overview. *Climatic Change*, **109**, 5, https://doi.org/10.1007/s10584-011-0148-z.

Visbeck, M. H., J. W. Hurrell, L. Polvani, and H. M. Cullen, 2001: The North Atlantic Oscillation: Past, present, and future.

Proc. Natl. Acad. Sci. USA, **98**, 12 876–12 877, https://doi.org/10.1073/pnas.231391598.

Wallace, J. M., and D. S. Gutzler, 1981: Teleconnections in the geopotential height field during the Northern Hemisphere winter. *Mon. Wea. Rev.*, **109**, 784–812, https://doi.org/10.1175/1520-0493(1981)109<0784:TITGHF>2.0.CO;2.

Wengel, C., S.-S. Lee, M. F. Stuecker, A. Timmermann, J.-E. Chu, and F. Schloesser, 2021: Future high-resolution El Niño/Southern Oscillation dynamics. *Nat. Climate Change*, **11**, 758–765, https://doi.org/10.1038/s41558-021-01132-4.

Westerling, A. L., 2016: Increasing western U.S. forest wildfire activity: Sensitivity to changes in the timing of spring. *Philos. Trans. Roy. Soc.*, **B371**, 20150178, https://doi.org/10.1098/rstb.2015.0178.

Williams, A. P., J. T. Abatzoglou, A. Gershunov, J. Guzman-Morales, D. A. Bishop, J. K. Balch, and D. P. Lettenmaier, 2019: Observed impacts of anthropogenic climate change on wildfire in California. *Earth's Future*, **7**, 892–910, https://doi.org/10.1029/2019EF001210.

Williams, I. N., and C. M. Patricola, 2018: Diversity of ENSO events unified by convective threshold sea surface temperature: A nonlinear ENSO index. *Geophys. Res. Lett.*, **45**, 9236–9244, https://doi.org/10.1029/2018GL079203.

Wills, R. C. J., R. H. White, and X. J. Levine, 2019: Northern Hemisphere stationary waves in a changing climate. *Curr. Climate Change Rep.*, **5**, 372–389, https://doi.org/10.1007/s40641-019-00147-6.

Wu, X., Y. M. Okumura, P. N. DiNezio, S. G. Yeager, and C. Deser, 2022: The equatorial Pacific cold tongue bias in CESM1 and its influence on ENSO forecasts. *J. Climate*, **35**, 3261–3277, https://doi.org/10.1175/JCLI-D-21-0470.1.

Yuan, J., B. Tan, S. B. Feldstein, and S. Lee, 2015: Wintertime North Pacific teleconnection patterns: Seasonal and interannual variability. *J. Climate*, **28**, 8247–8263, https://doi.org/10.1175/JCLI-D-14-00749.1.

Yun, K.-S., J.-Y. Lee, A. Timmermann, K. Stein, M. F. Stuecker, J. C. Fyfe, and E.-S. Chung, 2021: Increasing ENSO–rainfall variability due to changes in future tropical temperature–rainfall relationship. *Commun. Earth Environ.*, **2**, 43, https://doi.org/10.1038/s43247-021-00108-8.

Zhang, W., Z. Wang, M. F. Stuecker, A. G. Turner, F.-F. Jin, and X. Geng, 2019: Impact of ENSO longitudinal position on teleconnections to the NAO. *Climate Dyn.*, **52**, 257–274, https://doi.org/10.1007/s00382-018-4135-1.

Zhou, W., D. Yang, S.-P. Xie, and J. Ma, 2020: Amplified Madden–Julian Oscillation impacts in the Pacific–North America region. *Nat. Climate Change*, **10**, 654–660, https://doi.org/10.1038/s41558-020-0814-0.

Zhou, Z.-Q., S.-P. Xie, X.-T. Zheng, Q. Liu, and H. Wang, 2014: Global warming–induced changes in El Niño teleconnections over the North Pacific and North America. *J. Climate*, **27**, 9050–9064, https://doi.org/10.1175/JCLI-D-14-00254.1.